Case Studies in Construction Materials 24 (2026) e05973

Contents lists available at ScienceDirect

Case Studies in Construction Materials

journal homepage: www.elsevier.com/locate/cscm

Effects of ultrafine glass powder on the reliability analysis and life prediction of cement mortar under multi-concentration sulfate attack

Yuzhou Sun [a,b,*], Zhilong Li [c], Dongchang Hou [b,c], Yi Zhao [b,c], Jinyan Wang [b,c], Xiangming Zhou [d]

[a] School of Civil and Transportation Engineering, Henan University of Urban Construction, Pingdingshan 467036, China
[b] Henan Engineering Research Center of Mechanics and Engineering Structures, Zhongyuan University of Technology, Zhengzhou 451191, China
[c] School of Intelligent Construction and Civil Engineering, Zhongyuan University of Technology, Zhengzhou 450007, China
[d] Department of Civil and Environmental Engineering, Brunel University London, Uxbridge UB8 3PH, United Kingdom

ARTICLE INFO

Keywords:
Ultrafine Glass Powder
Sulfate Erosion
Nanoindentation
K-means Clustering Analysis
Weibull Distribution

ABSTRACT

In this paper, the influence mechanism of ultrafine glass powder (UGP) on the sulfate resistance of cement mortar is studied by replacing cement with different of equal quality amounts. The reliability analysis of UGP-modified cement mortar in sulfate environment is systematically discussed by mass change analysis, scanning electron microscope (SEM), X-ray diffraction (XRD) and nanoindentation, etc. The results show that the proper amount of UGP can significantly improve the sulfate resistance of cement mortar, and the effect is the best when the content of UGP is 10%. Compared with the undoped UGP group, the flexural strength and compressive strength increased by 11.34%, 8.62% and 6.63%, 6.85% respectively after 120 days of erosion in 5% and 10% sodium sulfate solutions, and the mass loss was the smallest. A two-parameter Weibull distribution model via relative dynamic elastic modulus is developed to predict the reliability life of UGP-modified cement mortar. The results show that 10% UGP content can significantly prolong the service life of cement mortar in sulfate environment. UGP effectively consumes $Ca(OH)_2$ through pozzolanic reaction, which promotes the formation of C-S-H gel and reduces the formation of expansion products such as gypsum ($CaSO_4 \cdot 2\ H_2O$) and ettringite (AFt), as well as optimizes pore structure and enhances material compactness and microscopic mechanical properties.

1. Introduction

Owing to their unique and irreplaceable advantages such as good barrier properties, corrosion resistance and acid corrosion resistance, glass products are widely used in many fields. Moreover, as a key daily necessity, glass is abundant in solid waste in many countries, mainly from daily life glassware, glass packaging materials and building glass [1–3]. With the rapid advancement of urbanization and infrastructure construction, the output of waste glass in cities continues to increase, but the rate of waste glass recycling is low [4]. Most glass residues are disposed off in landfills, which not only wastes land resources but also causes environmental

* Corresponding author at: School of Civil and Transportation Engineering, Henan University of Urban Construction, Pingdingshan 467036, China.
E-mail address: sunyz@zut.edu.cn (Y. Sun).

https://doi.org/10.1016/j.cscm.2026.e05973
Received 11 December 2025; Received in revised form 27 February 2026; Accepted 11 March 2026
Available online 12 March 2026

pollution [5]. Globally, the utilization rate of waste glass varies significantly. In many European countries, the recycling rate has reached approximately 70%, whereas in China it remains below 50% [6–8]. This low utilization rate not only represents a waste of resources but also poses environmental challenges. Converting waste glass into ultrafine powder as a supplementary cementitious material offers a promising solution [9–11]. UGP exhibits pozzolanic activity, which can enhance the densification of cement-based materials, inhibit alkali-silica reaction, and improve long-term durability [12–14]. However, the performance of UGP cement mortar under long-term erosion of different concentrations of sulfate has not been systematically studied, so comprehensive research is needed to fill this gap.

The durability of cement-based materials has always been the focus of research worldwide. In terms of durability, sulfate attack is among the main factors causing cement-based materials to fail [15–18]. At present, most coastal projects in coastal areas encounter sulfate attack. In addition, salinization in most parts of Northwest China is severe, and sulfate attack by cement-based materials is common [19–21]. To solve this problem, in recent decades, scholars worldwide have conducted many experimental studies [22–25]. Studies have shown that the incorporation of an appropriate amount of ultrafine admixture to replace some of the cement in the concrete production process can significantly improve its corrosion resistance. Commonly used ultrafine admixtures include fly ash, silica fume and slag powder. However, among the aforementioned materials, although silicon powder has the highest activity, it is not conducive to large-scale application because of its high price and limited production. Although slag powder and fly ash have good activity, their cost is still relatively high, second only to that of cement, and they are limited by the distribution of production areas, the high cost of use and the inconvenient supply in some areas [26–28]. In contrast, UGP is prepared from waste glass, with a wide range of sources and extremely low raw material costs. It has good pozzolanic activity when ground into ultrafine powder, which helps to improve the corrosion resistance of cement-based materials. For example, Peng et al. [29] proposed a low-carbon corrosion-resistant structural concrete that combines recycled aggregate concrete and GP and analysed the effects of the GP substitution ratio on the compressive strength of recycled aggregate concrete, chloride ion penetration resistance and the corrosion resistance of steel. Tahwia et al. [30] compared the mechanical properties, chloride ion permeability, carbonation resistance and high-temperature resistance of concrete mixed with ceramic waste powder, GP and granite waste powder with those of control concrete. The mechanical properties of low-carbon high-strength concrete with 10% GP and 20% granite waste powder were the greatest at 28 d. Cao et al. [31] reported that the incorporation of GP can significantly improve the sulfate resistance of a sample, and its improvement is closely related to the effect of the GP pozzolanic reaction on the pore solution composition and solid phase combination in the hydrated cement slurry.

In summary, the existing research focuses on the influence of mechanical properties and resistance to chloride ion permeability after incorporation of GP, and the particle size of GP used is mostly between 200 mesh and 500 mesh, which fails to reveal the sulfate resistance of ultra-fine glass powder cement mortar by combining macro and micro tests. Therefore, in this paper, UGP was used to prepare cement mortar specimens by replacing cement with equal mass, and the sulfate resistance of ultrafine glass powder cement mortar was studied. In order to further explore the influence mechanism of UGP content on the sulfate resistance of cement mortar, X-ray diffraction test (XRD), scanning electron microscope (SEM) and nanoindentation were used to analyze the evolution of hydration products, microstructure characteristics and micro-mechanical properties. The Weibull distribution was used to predict the life of UGP cement mortar, which provided a reference for its application in engineering.

2. Materials and experimental methods

2.1. Raw materials

2.1.1. Cement

P·O 42.5 ordinary Portland cement was used in this study. Its main chemical composition and physical properties are presented in Table 1 and Table 2, respectively. The particle size distribution of the cement is displayed in Fig. 1, with a median particle size of 13.86 μm.

2.1.2. Fine aggregate and water

The fine aggregate used in this study was ISO standard sand sourced from Xiamen ISO Standard Sand Co., Ltd. Its apparent density is 1350 kg/m^3, with a SiO_2 content exceeding 96%. The silt content is less than 0.2%, and the loss on ignition is less than 0.4%. The loose bulk density of the sand is 1611 kg/m^3. Laboratory tap water was used throughout the experiments.

2.1.3. Ultrafine glass powder

In order to prepare high purity UGP, colourless transparent waste glass bottles were used as raw materials. The flow chart of UGP preparation is shown in Fig. 2. The preparation process mainly includes the following steps:

Table 1
Main chemical composition of P·O 42.5 cement.

CaO	SiO_2	Al_2O_3	Fe_2O_3	MgO	SO_3	K_2O	Na_2O	total
61.52%	20.47%	5.55%	5.62%	3.41%	0.78%	1.28%	0.39%	97.9%

Table 2
Physical performance indexes of cement.

Index	Specific surface area (m^2/kg)	Density (g/cm^3)	Setting time (min)		Flexural strength (Mpa)		Compressive strength (Mpa)	
			Initial	Final	3d	28d	3d	28d
Value	353	3.03	221	276	4.6	7.38	22.4	45.5

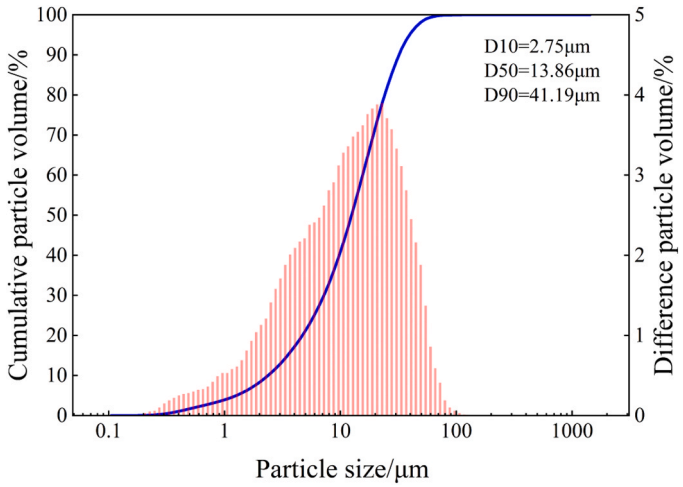

Fig. 1. Particle size of the cement.

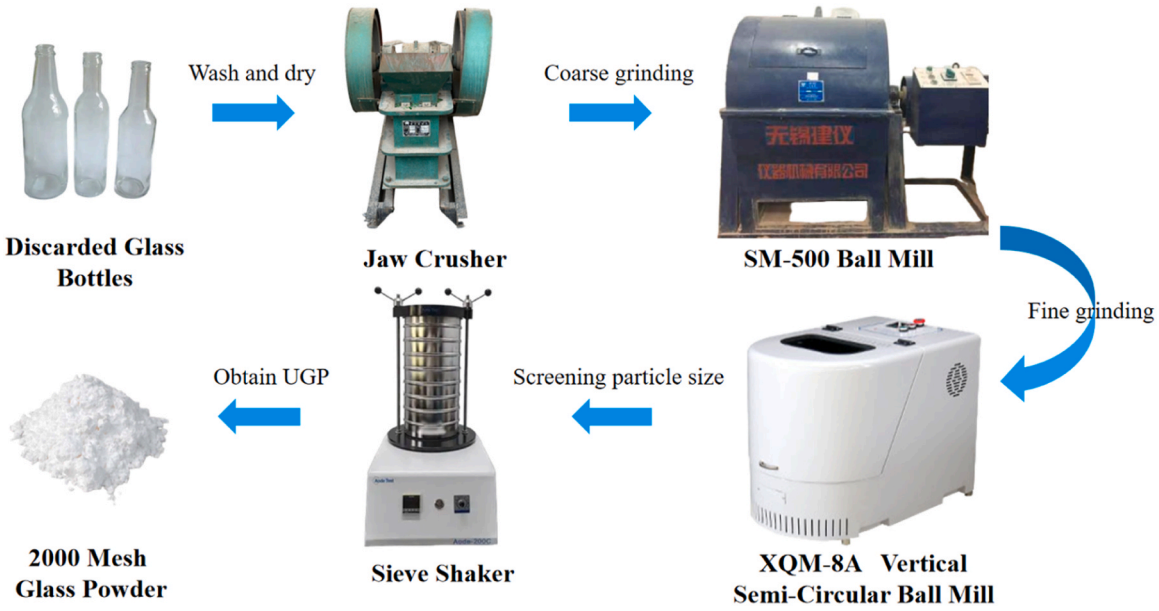

Fig. 2. UGP preparation flow chart.

(1) Raw material pretreatment: Colourless transparent waste glass bottles were cleaned, naturally dried to remove impurities, and then crushed into small pieces by a crusher.
(2) Rough grinding: Using SM-500 ball mill, the speed is 48 r/min, the grinding time is 30 min, and the coarse glass powder is obtained.
(3) Fine grinding: A vertical semi-circular planetary ball mill with a speed of 300 r/min and a grinding time of 4 h was used to further refine the powder.

(4) Screening: The final UGP was obtained by 2000 mesh standard screening. After the preparation of each batch of UGP, laser particle size analysis was performed to ensure that the particle size distribution of UGP was consistent.

The main chemical constituents of UGP are shown in Table 3. The particle size distribution of the UGP is presented in Fig. 3, which shows a median particle size of 7.12 μm. As shown in the SEM image in Fig. 4, the UGP particles had smooth surfaces and were angular.

2.1.4. Anhydrous sodium sulfate

Sodium sulfate powder of analytical reagent grade, with a purity of 99%, was obtained from Sinopharm Chemical Reagent Co., Ltd.

2.2. Preparation of mortar samples

In this test, four groups of mortar samples with a water–binder ratio of 0.5 were prepared by using a standard mix ratio. The specific mix ratios are shown in Table 4. NC represents the reference group; GC10, GC20 and GC30 represent the samples in which 10%, 20%, and 30% of cement is replaced with UGP of equal quality, respectively; and the test block has dimensions of 40 × 40 × 160 mm. First, the test block was demoulded after 1 day of natural curing, and the sulfate erosion test was subsequently conducted after 28 days of continuous curing in a standard curing box.

The sulfate corrosion resistance of the cement mortar samples was tested by following the Chinese standard “Test method for sulfate resistance of cement” (GB/T 749-2008) [32]. In this experiment, the full immersion method was used to place the test blocks with standard curing for 28 days in clear water, 5% sodium sulfate solution and 10% sodium sulfate solution to ensure that the solution height was at least 5 cm greater than that of the test block and that the mortar sample was completely immersed in the solution. The soaking periods were 0, 30, 60, 90 and 120 days, during which the sodium sulfate solution was replaced every 30 days to maintain its concentration. After the corresponding erosion cycle was reached, the mortar samples were removed, and the flexural strength, compressive strength, microstructure and corrosion products were tested. The production of mortar samples and the process of sulfate attack are shown in Fig. 5.

2.3. Flexural and compressive mechanical property tests

After the test age was reached, the mortar samples were removed from the water and sodium sulfate solution for flexural strength and compressive strength tests. The flexural strength and compressive strength were tested by referring to the “cement mortar strength test method (ISO method)” (GB/T 17671-2021) [33], and uniform loading was performed until the sample was destroyed. The formulas for calculating flexural strength and compressive strength are shown in Formulas (1) and (2), respectively.

$$R_f = \frac{1.5F_fL}{b^3} \tag{1}$$

$$R_c = \frac{F_c}{A} \tag{2}$$

where R_f is the flexural strength; F_f is the maximum load at fracture; in this experiment, L= 100 mm and b= 40 mm, R_c is the compressive strength, F_c is the maximum load at failure, and A is the clamping plate area, which is 1600 mm^2.

To better reflect the change in the strength of the mortar sample under sulfate attack, flexural and compressive corrosion resistance coefficients are introduced in this paper. The calculation methods are shown in Formulas (3) and (4).

$$K_f = \frac{R_{fs}}{R_{fo}} \tag{3}$$

$$K_c = \frac{R_{cs}}{R_{co}} \tag{4}$$

where K_f is the corrosion resistance coefficient of the mortar;, R_{fs} is the flexural strength of the mortar with different sulfate erosion durations, R_{fo} is the initial flexural strength of the mortar, K_c is the corrosion resistance coefficient of the mortar, R_{cs} is the compressive strength of the mortar with different sulfate attack durations;, and R_{co} is the initial compressive strength of the mortar.

2.4. Mass change test

The change in mortar quality in a sulfate environment can directly reflect the erosion of the sample. After the test was conducted,

Table 3
Main chemical compositions of UGP.

SiO_2	Na_2O	CaO	Al_2O_3	MgO	Others
72.68%	14.70%	4.35%	2.81%	0.93%	4.53%

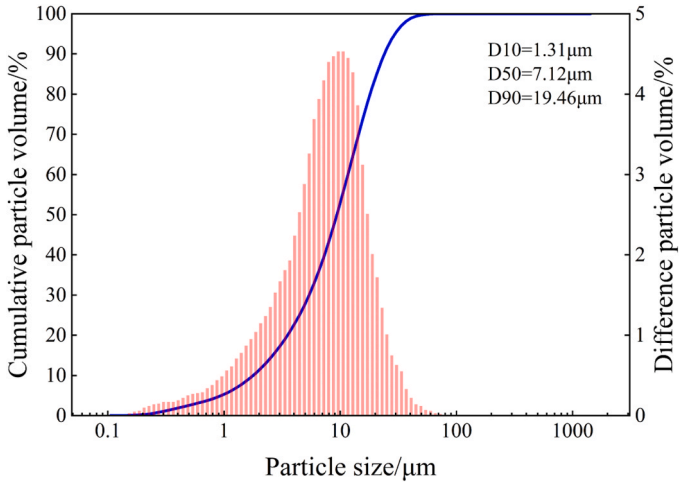

Fig. 3. Particle size distribution of the glass powder.

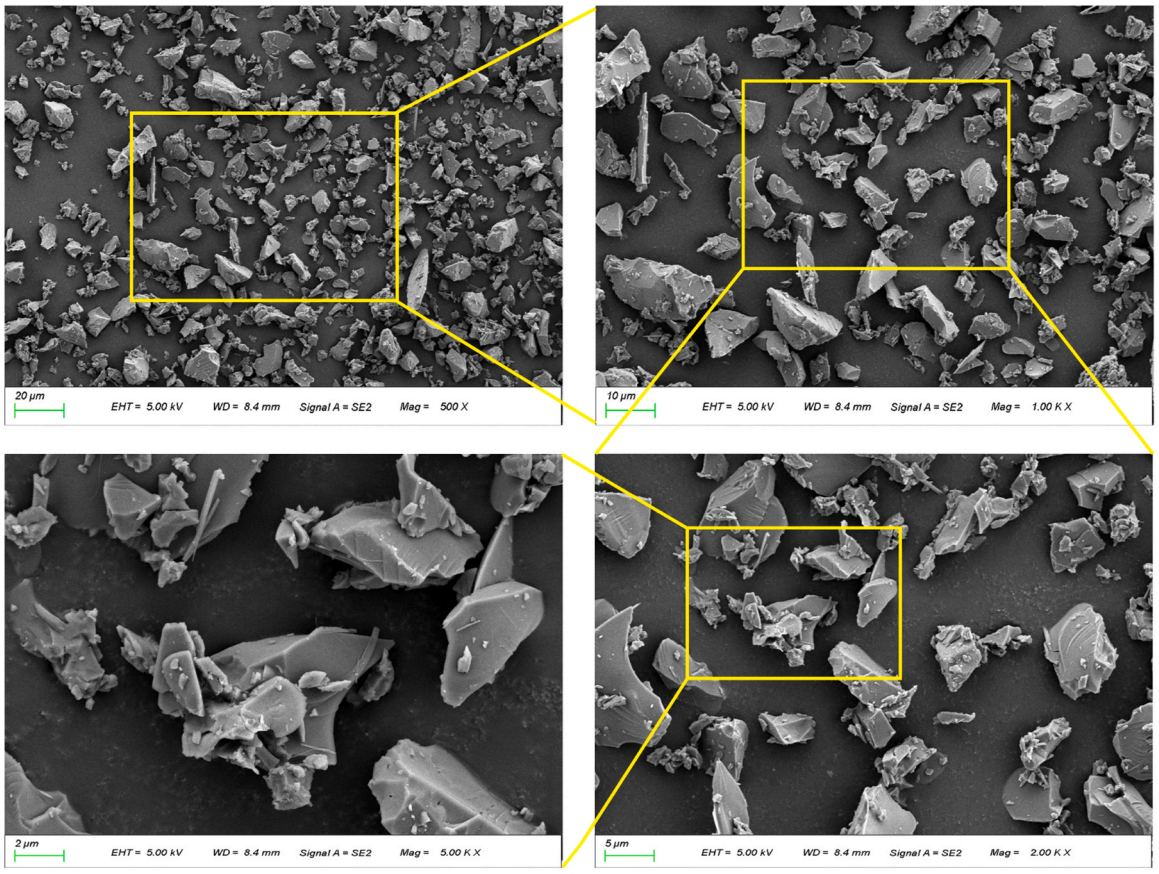

Fig. 4. Microstructure of the glass powder observed by SEM.

the samples were removed and dried in an oven at 50 °C for 48 h. After the test, the dry mass of the mortar was measured, and the average value was taken. The rate of change in the mortar mass was calculated according to Formula (5).

$$d_n = \frac{m_n - m_0}{m_0} \tag{5}$$

where d_n is the rate of change in the mass of the mortar sample after sulfate erosion for n days, m_n is the quality of the mortar sample

Table 4
Mixture proportions of the mortar samples.

Sample No.	Standard sand/g	Cement/g	Water/g	Glass powder/g
NC	1350	450	225	0
GC10	1350	405	225	45
GC20	1350	360	225	90
GC30	1350	315	225	135

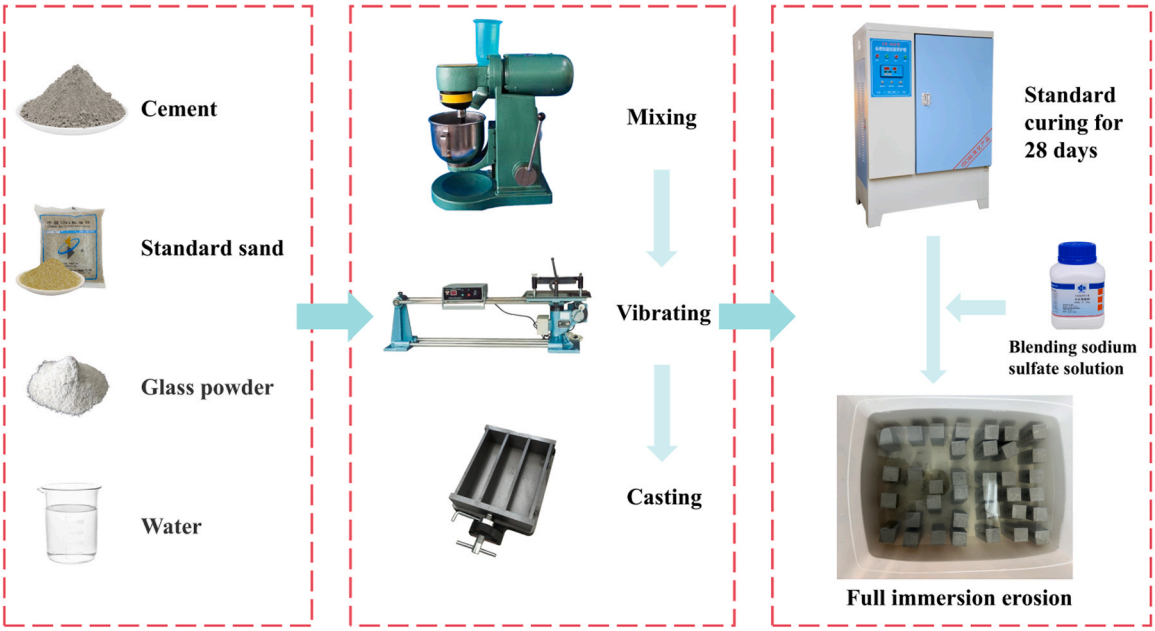

Fig. 5. Schematic diagram of mortar sample production and sulfate erosion.

after sulfate erosion for n days, and m_0 is the initial mass of the mortar.

2.5. Relative dynamic elastic modulus tests

In this experiment, the DT-20 dynamic elastic modulus tester was utilised to assess the longitudinal resonance frequency of mortar specimens with varying UGP contents, employing the resonance principle as the underlying method. The dynamic elastic modulus of the specimens was calculated after 5% and 10% sodium sulfate solution erosion at different ages. The relative dynamic elastic modulus is a key factor in the structural damage evolution law of mortar specimens under sulfate erosion. This index is also the core parameter for the subsequent establishment of Weibull distribution model to predict the reliability life of mortar. The calculation formula is as follows:

$$E_r = \frac{E_t}{E_0} \tag{6}$$

Where E_t denotes the dynamic elastic modulus measured after t days of sulfate erosion, and E_0 represents the corresponding modulus before the erosion test begins.

2.6. Microscopic morphology tests

The microstructure of and changes in the mortar samples after sulfate attack were analysed by scanning electron microscopy. The instrument used was a German ZEISS GeminiSEM 360 scanning electron microscope. The test samples were obtained from the same depth of different mortar crushing blocks after the compressive strength of the test piece was tested. The overall size of the sample was less than 0.5 cm, and the samples were as smooth as possible. The test samples were selected as follows: the NC group (NC-5–120), GC10 group (GC10–5–120), GC20 group (GC20–5–120), and GC30 group (GC30–5–120) samples were soaked in 5% sodium sulfate solution for 120 days. Before the test, the sample was dried, sprayed and vacuumized.

2.7. X-ray diffraction tests

A German Bruker D8Advance X-ray diffractometer was used for the X-ray diffraction test. The position used to test the samples was the same for the NC-5–120, GC10–5–120, GC20–5–120 and GC30–5–120 groups. After the samples were dried to a constant weight, the samples were ground into powder with an agate mortar until there were no visible particles, after which the ground mortar sample powder was sieved through a 75 μm sieve. A copper target was used, the scanning speed was 2°/min, and the scanning angle range was $5^\circ \leq 2\theta \leq 90^\circ$.

2.8. Nanoindentation tests

2.8.1. Sample preparation

First, the mortar blocks of the NC-5–120, GC10–5–120, GC20–5–120 and GC30–5–120 groups were cut into small pieces with dimensions of 1 cm × 1 cm × 1 cm by using a special cutting machine. After cutting, the samples were soaked in anhydrous ethanol for 2 days to terminate the hydration reaction. Afterwards, the sample was removed from anhydrous ethanol, dried, and placed in the centre of the circular soft mould. After the solution was prepared with epoxy resin and a curing agent, the sample was slowly stirred to solidify the sample and then demoulded after allowing to stand for 5 h. Then, the demoulded samples were placed in a metallographic grinding and polishing machine, and the samples were polished with 200, 600, 1500, 2000 and 4000 mesh sandpaper until the surface of the samples was exposed. The duration of grinding with the 200 mesh and 600 mesh sandpaper did not exceed 5 min, and the duration of grinding corresponding to the remaining mesh sandpaper was not less than 30 min. Subsequently, the sample was polished with a polymer synthetic leather polishing cloth, and the polished sample was polished with 3μm, 1μm, and 0.3μm diamond suspensions in turn. The duration of polishing with each diamond suspension was not less than 30 min. Finally, the polished sample was placed in an ultrasonic cleaner for cleaning, and the duration of cleaning was not less than 5 min.

2.8.2. Theoretical basis

The nanoindentation instrument used in this experiment was an Agilent G200 nanoindentation instrument (United States). The load and displacement resolutions were 50 nN and 0.01 nm, respectively. The indenter used in the instrument was a Berkovich diamond indenter. In the experiments, the maximum indentation depth of the instrument indenter was set to 2000 nm, and the thermal drift index of the instrument was 0.05 nm/s. Each experiment used 10 × 10 lattice for indentation test, a total of 100 indentation points. After eliminating invalid points and unhydrated points, additional points are randomly added in the original area to ensure that each sample has exactly 100 valid and representative data points. The indentation spacing between adjacent indentation points is 10 μm. The distribution diagram of nanoindentation test points is shown in Fig. 6.

Nanoindentation technology is an advanced microscopic measurement technology that was recently developed and that can measure the elastic modulus, hardness and creep properties of materials at the nanoscale. Oliver et al. [34] established a theory of elastic modulus and hardness analysis on the basis of nanoindentation curves. With the nanoindentation technique, the load−depth (F−h) curve is obtained by pressing an indenter with a specific shape onto the surface of the material, and the microscopic mechanical properties of the material are analysed on the basis of the theory of contact mechanics to calculate the contact reduction modulus (E_r) and indentation hardness (H) of the material [35]:

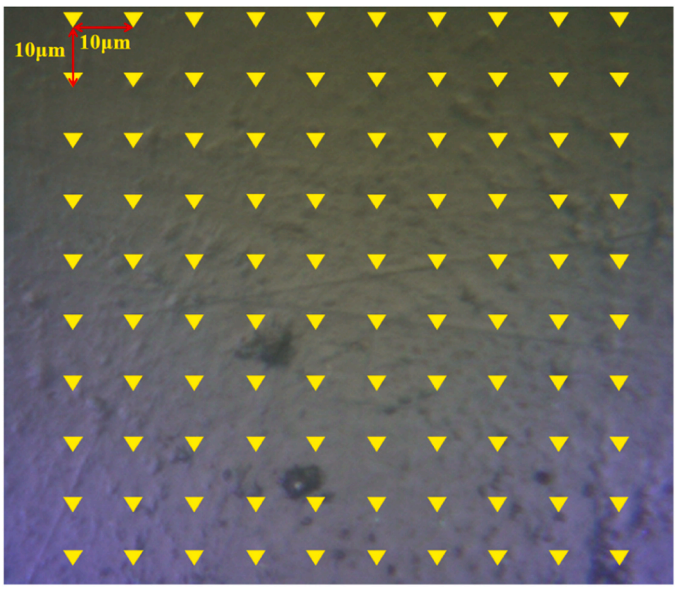

Fig. 6. Distribution of nanoindentation test points.

$$E_r = \frac{\sqrt{\pi}}{2\beta\sqrt{A_c}}S \tag{7}$$

$$H = \frac{F}{A_c} \tag{8}$$

$$S = \frac{dF}{dh}|h_{\max} \tag{9}$$

where β is a dimensionless correction coefficient related to the indenter. The indenter used in this test was a Berkovich diamond indenter, with β= 1.05; S is the indentation unloading stiffness, N/m; and A_c is the area of contact at the maximum indentation depth (h_{max}), nm^2, which is a function of the contact depth (h_c) at h_{max}.

For isotropic homogeneous materials, E_r can be calculated by Eq. (10).

$$\frac{1}{E_r} = \frac{(1-\upsilon^2)}{E} + \frac{(1-\upsilon_i^2)}{E_i} \tag{10}$$

where υ is the Poisson's ratio of the measured material; E is the elastic modulus of the measured material, GPa; υ_i is the Poisson's ratio of the indenter; and E_i is the elastic modulus of the indenter, GPa.

2.8.3. Data processing

Nanoindentation data are processed via cluster analysis, which is an unsupervised learning method. Common clustering approaches based on Euclidean distance include the K-means algorithm and K-medoids algorithm [36]. The objective of cluster analysis is to partition data samples into several disjoint subsets, each referred to as a "cluster". Each cluster embodies a latent concept or category. For the nanoindentation data, a cluster represents a specific phase within the hydration products. Typically, cementitious mortar minerals can be classified into a porous composite phase (PP), low-density calcium silicate hydrate (LD C–S–H), high-density calcium silicate hydrate (HD C–S–H), calcium hydroxide (CH), and unhydrated phases [37]. This study focuses solely on the pore and hydration phases and disregards the unhydrated phases. Representative F–h curves for different phases are shown in Fig. 7.

In this paper, K-means clustering analysis is used. The principle of K-means clustering analysis is as follows [38]: First, K points are randomly selected as the initial clustering centre. The value of K represents the final number of clustering categories. The K value in this paper is 4. Afterwards, the distance from each sample point to the centre is calculated and divided into the cluster where the nearest centre point μ^j, where $j \in \{1,\ldots,k\}$, is located, and the clustering centre of each cluster is subsequently recalculated. This step is repeated until the centre position remains unchanged or a predetermined number of iterations is reached. The K-means clustering process is shown in Fig. 8. The objective function of the algorithm is the within-cluster sum of squared errors (SSE), and the calculation formula is as follows:

$$SSE = \sum_{i=1}^{n}\sum_{j=1}^{k} \omega^{(i,j)} \left\| x^i - \mu^j \right\|^2 \tag{11}$$

If sample point x^i belongs to Cluster j, then $\omega^{(i,j)}$= 1; otherwise, it is 0.

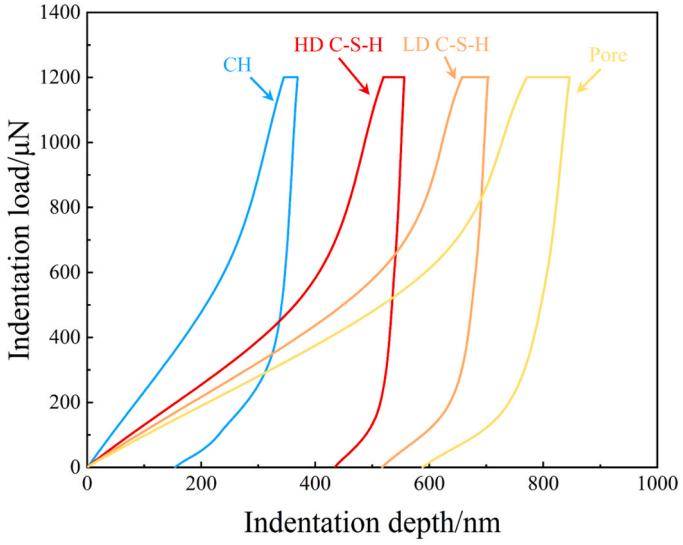

Fig. 7. F–h curves for different phases.

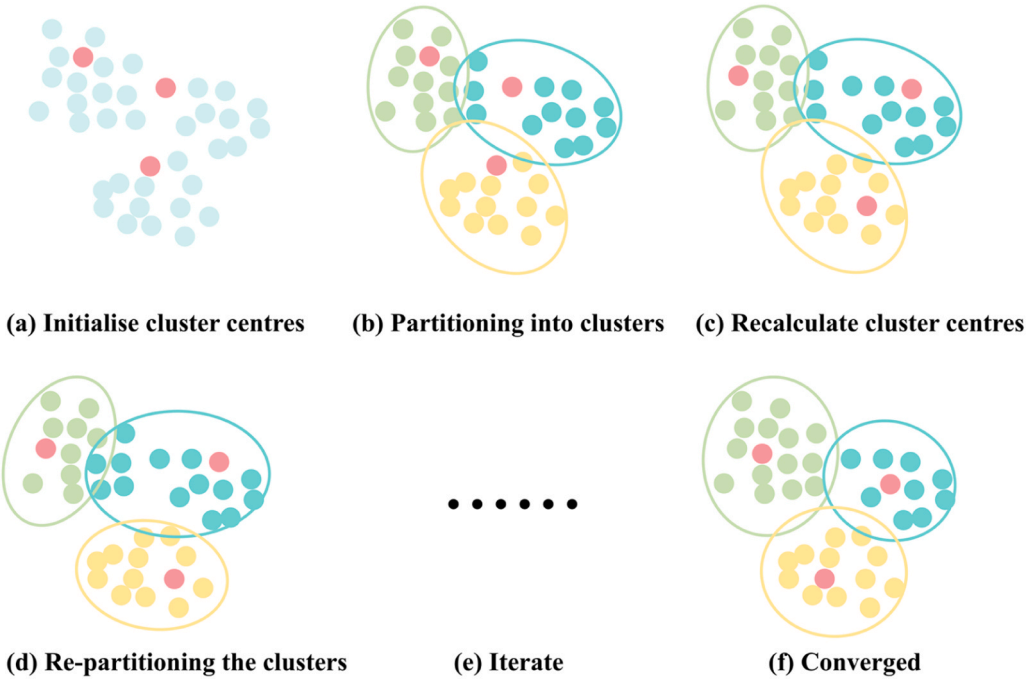

Fig. 8. K-means clustering process.

3. Results and analysis

3.1. Analysis of mechanical properties

The changes in the flexural strength and compressive strength of the mortar samples under sulfate attack at different concentrations are shown in Fig. 9. As shown in Fig. 9, with increasing erosion time and sulfate concentration, the flexural strength and compressive strength of the samples first increased but then decreased. The flexural strengths of the NC, GC10, GC20 and GC30 samples without sulfate attack were 7.38, 7.80, 7.00 and 6.73 MPa, respectively, and the compressive strengths were 45.50, 47.26, 44.53, and 43.16 MPa, respectively, after 28 days of standard curing. The flexural strength of the GC10 group was 5.7% greater than that of the NC group, and the compressive strength increased by 3.9%. Compared with that of the NC group, the flexural strengths of the GC20 and GC30 groups decreased by 5.1% and 8.8%, respectively, and the compressive strengths decreased by 2.1% and 5.2%, respectively.

Under erosion in a clear water environment, the flexural strength and compressive strength of the NC, GC10, GC20 and GC30 groups of mortar samples peaked at 60 days (Fig. 9(a)). The flexural strengths were 9.76, 10.73, 8.89 and 8.23 MPa, and the compressive strengths were 55.1, 58.93, 52.63, and 49.97 MPa, respectively. This trend is due to the cement hydration reaction occurring 60 days before soaking and the continuous progress of UGP pozzolanic effect reaction to produce producing a large number of hydration products. After the 60 days of soaking age is greater than 60 days, the cement has completed the hydration reaction was complete, and the strength of the sample no longer improved.

As shown in Fig. 9(b), under erosion in a 5% sodium sulfate solution, the flexural strength and compressive strength of all the mortar samples first increased but then decreased, which is directly related to the two-stage “filling enhancement–expansion failure” of sulfate erosion [39–41]. During the initial stage of erosion (0–60 days), sulfate ions slowly invaded the interior of the sample, reacted with the cement hydration product $Ca(OH)_2$ to form gypsum, and reacted with hydrated calcium aluminate to form AFt. A small amount of gypsum and AFt generated at the initial stage filled the primary pores inside the sample, resulting in a “filling enhancement effect”, so the strength of each group tended to increase. At this time, the peak flexural strength of the NC group was 9.63 MPa, and the compressive strength was 52.12 MPa; the peak flexural strength and compressive strength of the GC10 group were 10.4 MPa and 55.83 MPa, respectively, which were greater than those of the NC group. The peak flexural strengths of the GC20 and GC30 groups were 8.81 and 8.39 MPa, respectively, and the compressive strengths were 49.73 and 47.39 MPa, respectively, which were lower than those of the NC group. In the later stage of erosion (90–120 days), with the continuous advancement of sulfate erosion, large amounts of AFt and gypsum were generated inside the sample. Volume expansion caused microcracks to form inside the sample, and crack propagation caused the strength to enter the decreasing stage. At this time, the strength of the GC10 group also decreased, but its strength was always greater than that of the NC group, whereas the strengths of the GC20 and GC30 groups were always less than those of the NC group. The results show that the addition of 10% UGP can decrease the rate of sulfate ion intrusion by increasing the compactness of the sample. The pozzolanic reaction of UGP consumes some of the $Ca(OH)_2$ and reduces the amount of gypsum and AFt, and the generated C−S−H gel further densifies the structure of the sample and hinders the deep intrusion of sulfate ions [42–44].

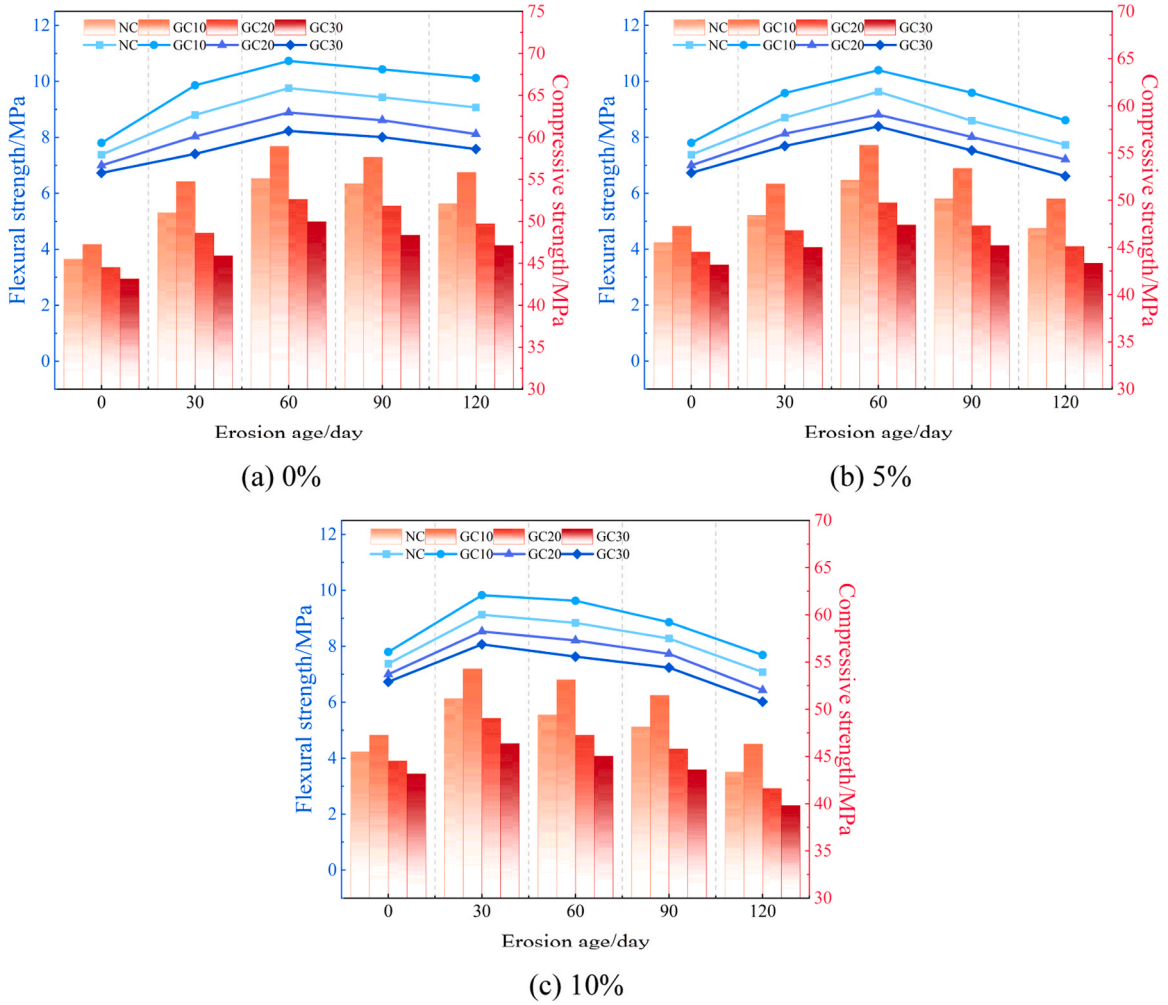

Fig. 9. Flexural strength and compressive strength of mortar samples under erosion by sodium sulfate solutions of different concentrations.

However, at high substitution rates of 20% and 30%, the amount of cement was insufficient, the total amount of early hydration products decreased, the initial porosity of the sample increased, sulfate ions were more likely to penetrate the interior, and the large number of expansion products in the later period caused more severe internal damage and a greater decrease in strength.

As shown in Fig. 9(c), with erosion in the high-concentration 10% sodium sulfate solution, the sulfate erosion effect strengthened, and the strength of each mortar sample peaked at first but then decreased rapidly in the later stage. The strength of each mortar sample peaked after 30 days of erosion, and the overall strength was less than that of the sample eroded in 5% sodium sulfate solution. The strength of the GC10 group was still greater than that of the NC group during the same period, indicating that even in a high-concentration erosion environment, 10% UGP can play an anti-erosion role by improving the compactness of the sample and inhibiting the formation of expansion products.

Fig. 10 presents the flexural and compressive corrosion resistance coefficients of mortar samples under sodium sulfate erosion at different concentrations, where the evolution of these coefficients is governed by the combined effects of the erosion environment and the UGP replacement ratio. In a clear water environment with 0% sodium sulfate, the corrosion resistance coefficients of all groups increased steadily, peaked at 60 days, and then declined gradually; after 120 days of immersion, the GC10 group exhibited flexural and compressive corrosion resistance coefficients of 1.38 and 1.25, respectively, which were higher than those of the NC group (1.32 and 1.21), the GC20 group (1.27 and 1.18), and the GC30 group (1.22 and 1.16), confirming that the mortar with a 10% UGP replacement ratio achieved the optimal synergistic effect between cement hydration and the pozzolanic reaction of UGP. Under 5% sodium sulfate erosion, the corrosion resistance coefficients of all groups showed an initial increase followed by a decrease, reaching their maximum at 60 days before declining rapidly; after 120 days of erosion, the NC group demonstrated flexural and compressive corrosion resistance coefficients of 1.05 and 1.03, while the GC10 group maintained higher coefficients of 1.11 and 1.06, whereas the GC20 and GC30 groups recorded lower flexural and compressive corrosion resistance coefficients, namely 1.03 and 0.98 for GC20, and 1.01 and 1.01 for GC30, respectively, indicating that the 10% UGP replacement contributed to a denser microstructure that delayed expansion damage, while higher replacement ratios accelerated erosion due to increased initial porosity. Under 10% high-concentration erosion,

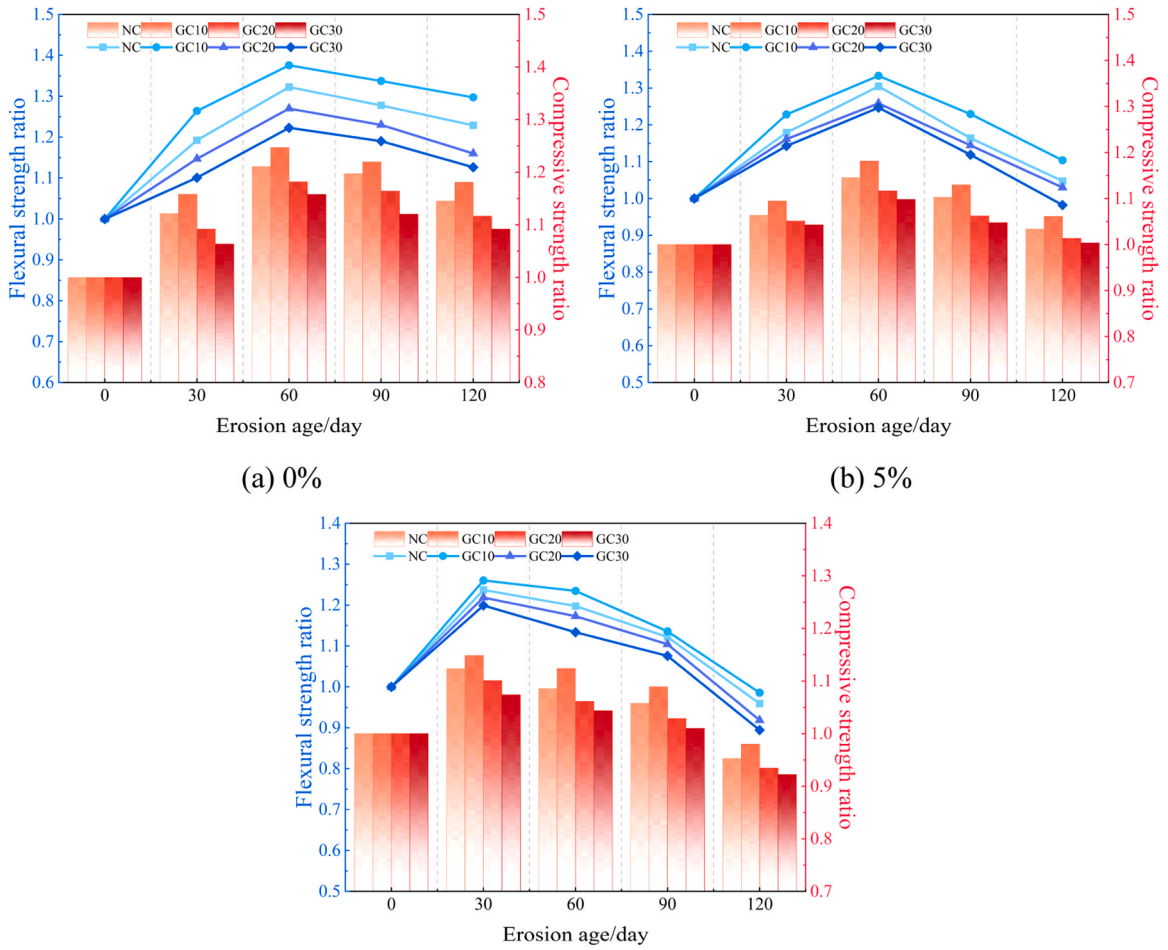

Fig. 10. Flexural corrosion resistance coefficient and compressive corrosion resistance coefficient of mortar samples under erosion by sodium sulfate solutions of varying concentrations.

the peak corrosion resistance coefficients occurred earlier, at 30 days, followed by a sharp decline; after 120 days of immersion, the GC10 group showed flexural and compressive corrosion resistance coefficients of 0.99 and 0.98, closely matching those of the NC group (0.96 and 0.95), further demonstrating that samples with a 10% UGP replacement retained comparatively good erosion resistance even under severe sulfate attack.

3.2. Quality change analysis

The rates of change in the mass of the mortar samples immersed in 0%, 5% and 10% sodium sulfate solutions for 0–120 d are shown in Fig. 11(a), (b) and (c), respectively. As shown in Fig. 11(a), the rate of change in the mass of each group of samples tended to increase but then gradually decreased, and the peak occurred at 60 d of erosion. After 60 days of erosion, the highest rate of change in the mass of the GC10 group was 0.056, which was higher than that of the NC group (0.053) and those of the GC20 and GC30 groups (0.051 and 0.048, respectively). This phenomenon originates from the clear water environment, and the change in the quality of the sample was dominated only by cement hydration and UGP pozzolanic reactions: C−S−H gel continued to be generated, the primary pores in the sample were filled, the compactness of the sample was improved, and the quality of the sample slowly increased; because the GC10 group contained the greatest amount of the C−S−H gel and the pore filling effect was the greatest, the rate of increase in mass was greatest. Owing to the decrease in the cement content, the total amount of hydration products in the GC20 and GC30 groups was insufficient, the amount of gel formed by the pozzolanic reaction was limited, and the rate of increase in mass was lower than that in the GC10 group. With increasing erosion duration, the hydration reaction of the cement was completed, and long-term immersion caused a small amount of fragments to fall off the surface of the sample; thus, the rate of change in the mass of each group of samples began to decrease gradually [45].

As shown in Fig. 11(b), the rate of change in the mass of samples in each group immersed in the 5% sodium sulfate solution first increased but then decreased. After 120 days of erosion, the mass loss of the GC10 group was the lowest at 0.2%, followed by that of the NC group at 2.2%. In contrast, the GC20 and GC30 groups presented the most significant losses at 3.1% and 4.3%, respectively.

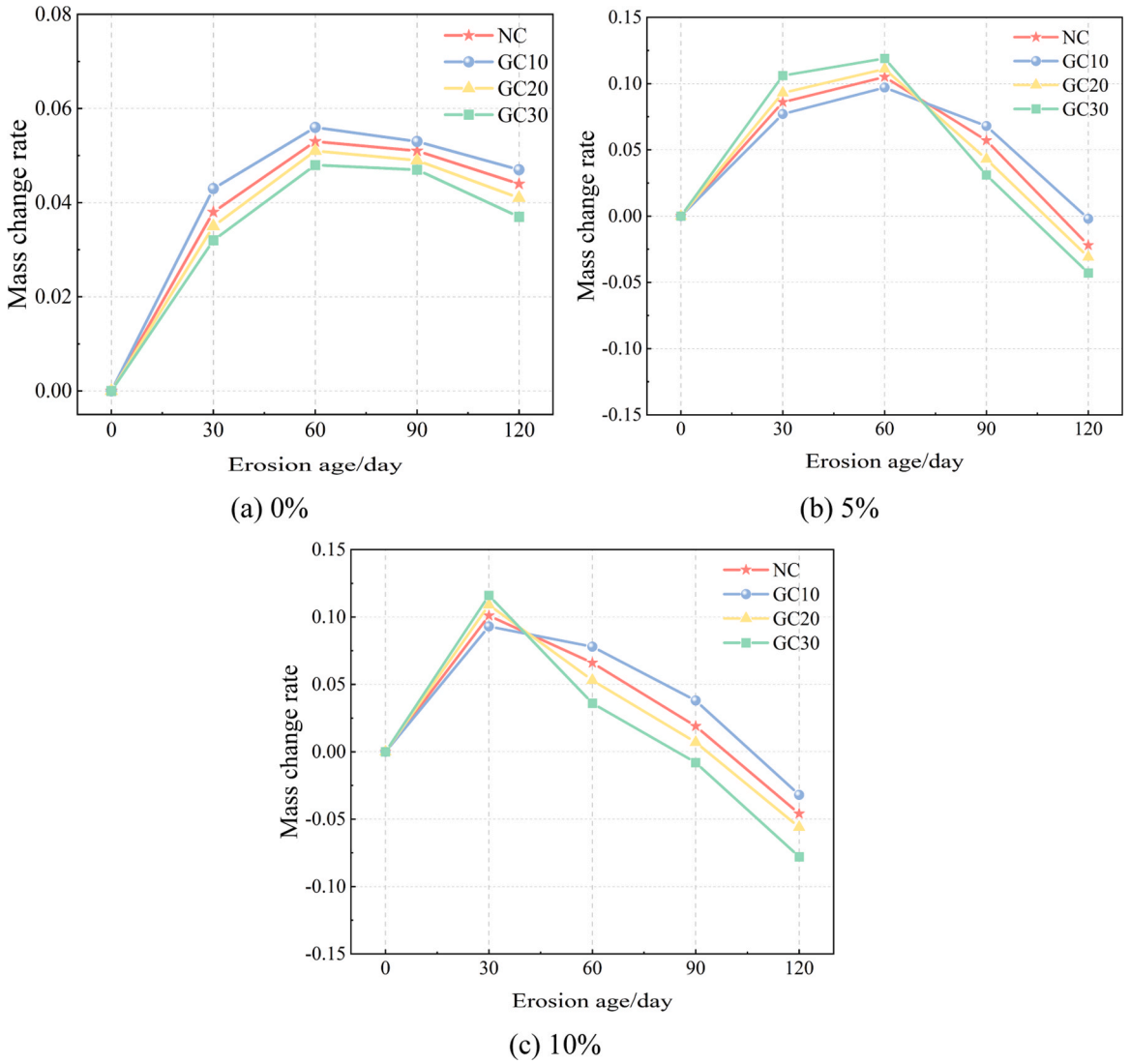

Fig. 11. Rate of change in the mass of the mortar samples under erosion by sodium sulfate solutions with different concentrations.

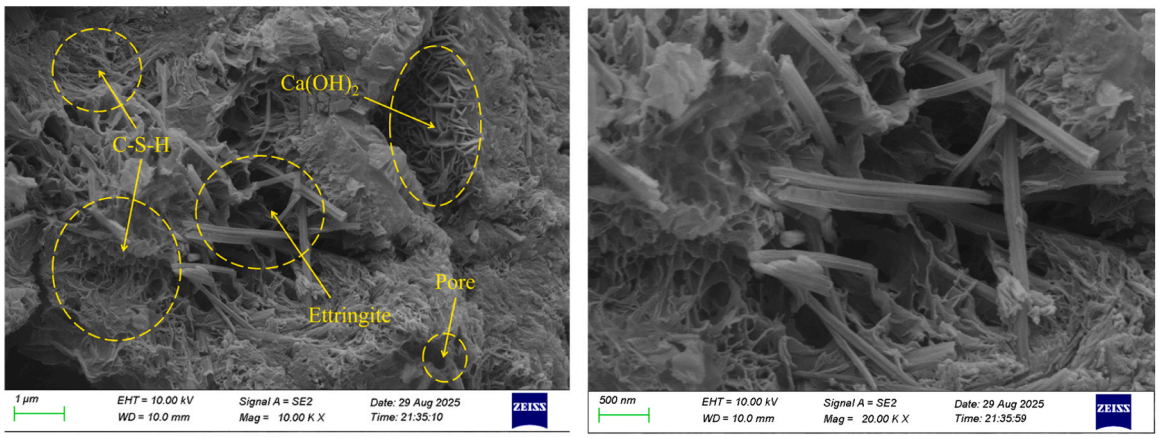

Fig. 12. SEM images of the mortar samples in the NC group eroded in 5% sodium sulfate solution for 120 days.

Analysis indicated that during the initial erosion period (0–60 days), sulfate ions penetrated the samples, reacting with the cement hydration product $Ca(OH)_2$ to form gypsum and with calcium aluminate hydrates to form AFt. These two erosion products filled the pores, increasing the sample mass. After erosion for 90–120 days, the volume expansion caused by excess gypsum and AFt induced the formation of microcracks within the samples. The propagation of these cracks led to a decrease in the sample mass [46].

As shown in Fig. 11(c), under the action of a 10% sodium sulfate solution, the rate of change in the mass of each group of samples peaked at 30 d. By day 120, the mass losses of the samples in groups GC20 and GC30 were large, with the masses decreasing by 5.6% and 7.8%, respectively, while the mass loss of the samples in the GC10 group was only 3.2%. In the GC10 samples, some of the $Ca(OH)_2$ was consumed because of the pozzolanic reaction, reducing the amounts of gypsum and Aft produced, and the C−S−H gel further densified the structure of the sample, which delayed the penetration of sulfate ions and the development of cracks and resulted in the smallest mass loss [47]; in the GC20 and GC30 groups, owing to the high rate of UGP substitution and the insufficient amount of cement, the initial porosity was higher, the sulfate ions were more likely to penetrate the interior, the expansion-induced damage in the later stage was more severe, and mass loss was aggravated. This finding is similar to the results obtained in Section 3.1.

3.3. Micromorphology analysis

The micromorphologies of the NC, GC10, GC20 and GC30 groups of mortar samples eroded for 120 days in a 5% sodium sulfate solution are shown in Figs. 12, 13, 14 and 15, respectively. In the NC group without UGP (Fig. 12), flaky $Ca(OH)_2$ crystals and needle-like AFt aggregates were observed, the structure was loose, and obvious microcracks and holes were present, indicating that under long-term sulfate attack, the continuous formation of gypsum and AFt led to volume expansion and internal structural damage. By contrast, as shown in Fig. 13, the structure of the GC10 group was more compact, the number of $Ca(OH)_2$ crystals reduced, the C−S−H gel was continuously distributed, and the number of cracks and holes was lower, indicating that the volcanic ash reaction of UGP effectively consumed part of the $Ca(OH)_2$ and inhibited the formation of expansive products. Moreover, the generated C−S−H gel further filled the pores and increased the compactness and erosion resistance of the system. This dense microstructure directly contributes to the higher flexural and compressive strengths observed in Fig. 9.

With increasing UGP content, the microstructure inside the sample obviously deteriorated, as shown in Fig. 14 and Fig. 15 In the GC20 group, the expansion-induced damage caused by AFt and gypsum led to the structural weakening and a decrease in the amount of the C−S−H gel inside the sample, and the gel dissolved. Many holes remained, and compared with that of the NC group, the microstructure was more degraded. In the GC30 sample, a large number of well-developed needle-like AFt and gypsum structures appeared inside the sample and were interspersed in the cracks and pores. The internal microstructure of the sample was severely degraded, no obvious flocculent C-S-H gel existed, indicating that an insufficient amount of cement caused the internal structure of the sample to be loose, and the pozzolanic reaction failed to fully compensate for the pore defects. Sulfate ions are more likely to invade and generate a large amount of AFt and gypsum inside, aggravating the expansion-induced damage.

In summary, SEM analysis verified that, at the microscopic level, 10% UGP delayed sulfate attack by optimizing the composition of the hydration products and pore structure. However, too high of a content leads to a decrease in corrosion resistance because of initial structural defects and insufficient reactions.

3.4. XRD analysis

The XRD patterns of different mortar samples eroded for 120 days in a 5% sodium sulfate solution are shown in Fig. 16. The XRD data clearly showed the phase differences in different groups of samples after long-term sulfate attack. The characteristic peaks of silica were detected in all the groups and were derived mainly from standard sand and UGP. In the NC group, strong $Ca(OH)_2$ diffraction peaks and obvious characteristic peaks of AFt and $CaSO_4 \cdot 2\,H_2O$ can be observed. This shows that after sulfate ions penetrated the

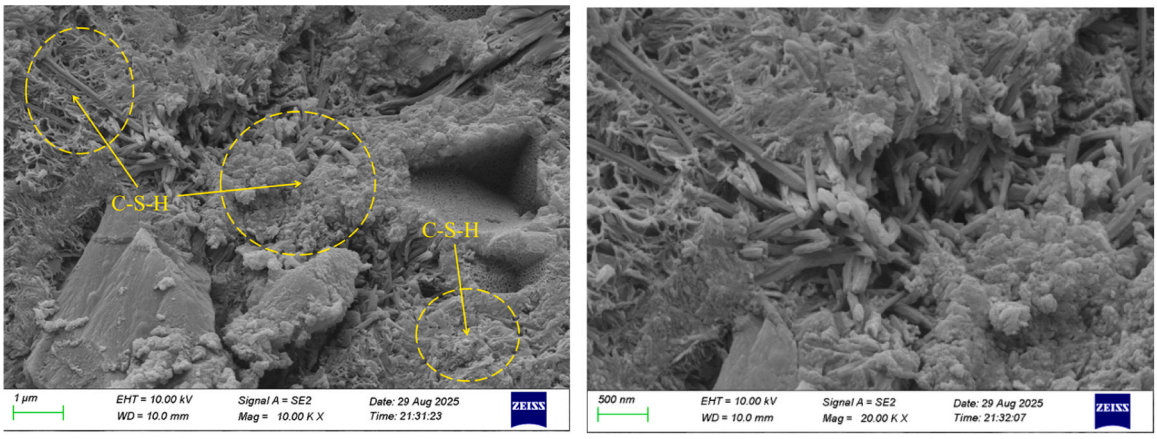

Fig. 13. SEM images of the mortar samples in the GC10 group eroded in a 5% sodium sulfate solution for 120 days.

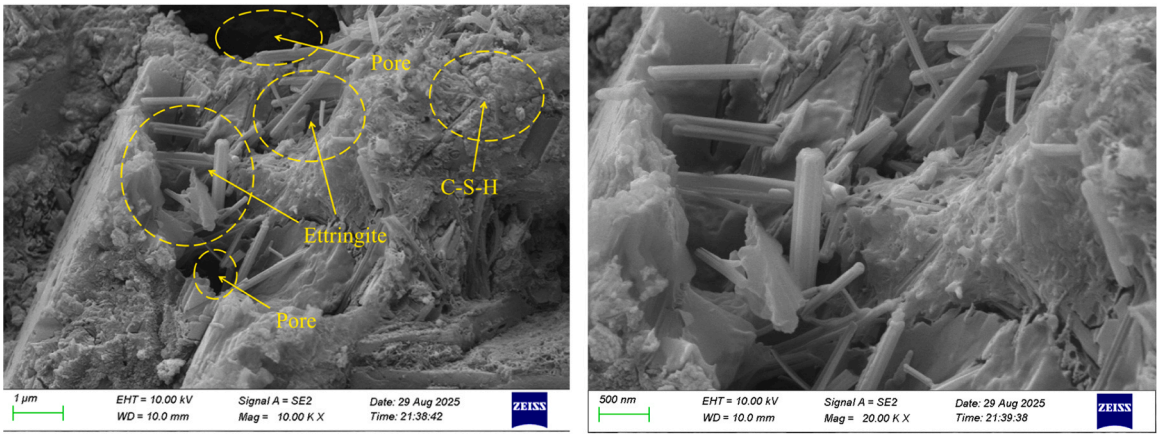

Fig. 14. SEM images of the mortar samples in the GC20 group eroded in 5% sodium sulfate solution for 120 days.

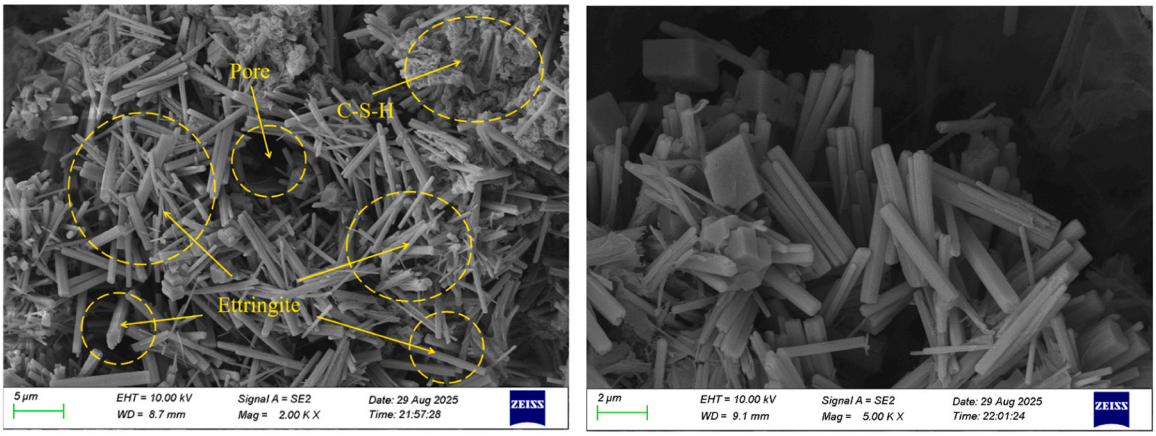

Fig. 15. SEM images of the mortar samples in the GC30 group eroded in 5% sodium sulfate solution for 120 days.

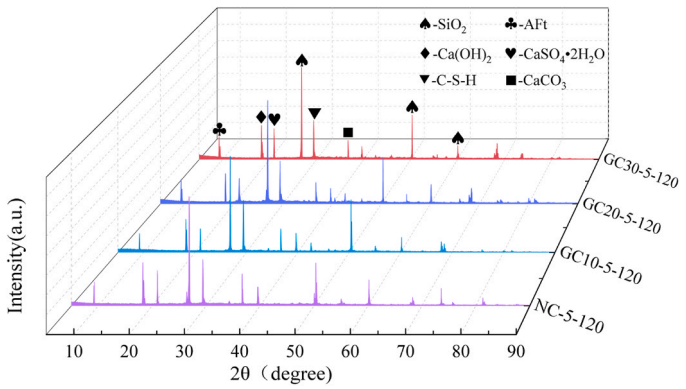

Fig. 16. XRD patterns of different mortar samples after 120 days of erosion in 5% sodium sulfate.

cement mortar in the NC group, the ions reacted with the hydration product $Ca(OH)_2$ to form a large amount of gypsum and simultaneously reacted with the hydrated calcium aluminate to form a large amount of AFt. The enrichment of these crystalline expansion products was the direct cause of the microstructure cracking and the degradation in the macroscopic performance of the NC group. In contrast to that in the GC10 group, the intensity of the $Ca(OH)_2$ diffraction peak decreased significantly, and the diffraction peaks of AFt and $CaSO_4{\cdot}2\ H_2O$ were also relatively weakened. This phenomenon proves the effectiveness of the UGP pozzolanic reaction: the active SiO_2 in UGP reacts with $Ca(OH)_2$ in the system, consuming some of the $Ca(OH)_2$ and thus reducing the amount of reactants

available for the formation of gypsum and AFt, two key expansion products. The reduction in $Ca(OH)_2$ and expansion products, combined with the denser C-S-H matrix, explains the improved mechanical performance of the GC10 group.

For the samples in the GC20 and GC30 groups, although the intensity of the $Ca(OH)_2$ peak decreased, the diffraction peaks of AFt and $CaSO_4 \cdot 2\,H_2O$ did not decrease in intensity. This finding indicates that at high amounts, the loose internal structure of the sample caused by the reduction in the amount of cement material provided a channel for the rapid invasion of sulfate ions, resulting in the continuous generation of AFt and $CaSO_4 \cdot 2\,H_2O$. Although the C−S−H gel can be generated by pozzolanic reactions, the amount formed is insufficient to offset the negative impact caused by the lack of cementitious materials and the internal structural defects of the sample, which ultimately aggravates erosion damage.

3.5. Nanoindentation analysis

The K-means clustering results of different mortar samples eroded in 5% sodium sulfate solution for 120 days are shown in Fig. 17. The results of the cluster analysis of the hardness and elastic modulus of different mortar samples are listed in Table 5. The micromechanical properties of the GC10 group were the best. The volume fraction of the HD C−S−H phase was 48%, whereas the volume fraction of the PP phase was reduced to 11%, and the volume fraction of the CH phase was also reduced to 14%. These results confirm that the addition of 10% UGP promotes the formation of a high-density C−S−H gel through an effective pozzolanic reaction and optimizes the pore structure inside the sample; thus, the sample has a higher elastic modulus and hardness and improved corrosion resistance.

By contrast, in the NC group, the HD C–S–H phase accounted for 35%, whereas the PP phase accounted for 14%, and the CH phase accounted for 18%. The proportion was greater, resulting in the overall micromechanical properties of the sample being weaker than

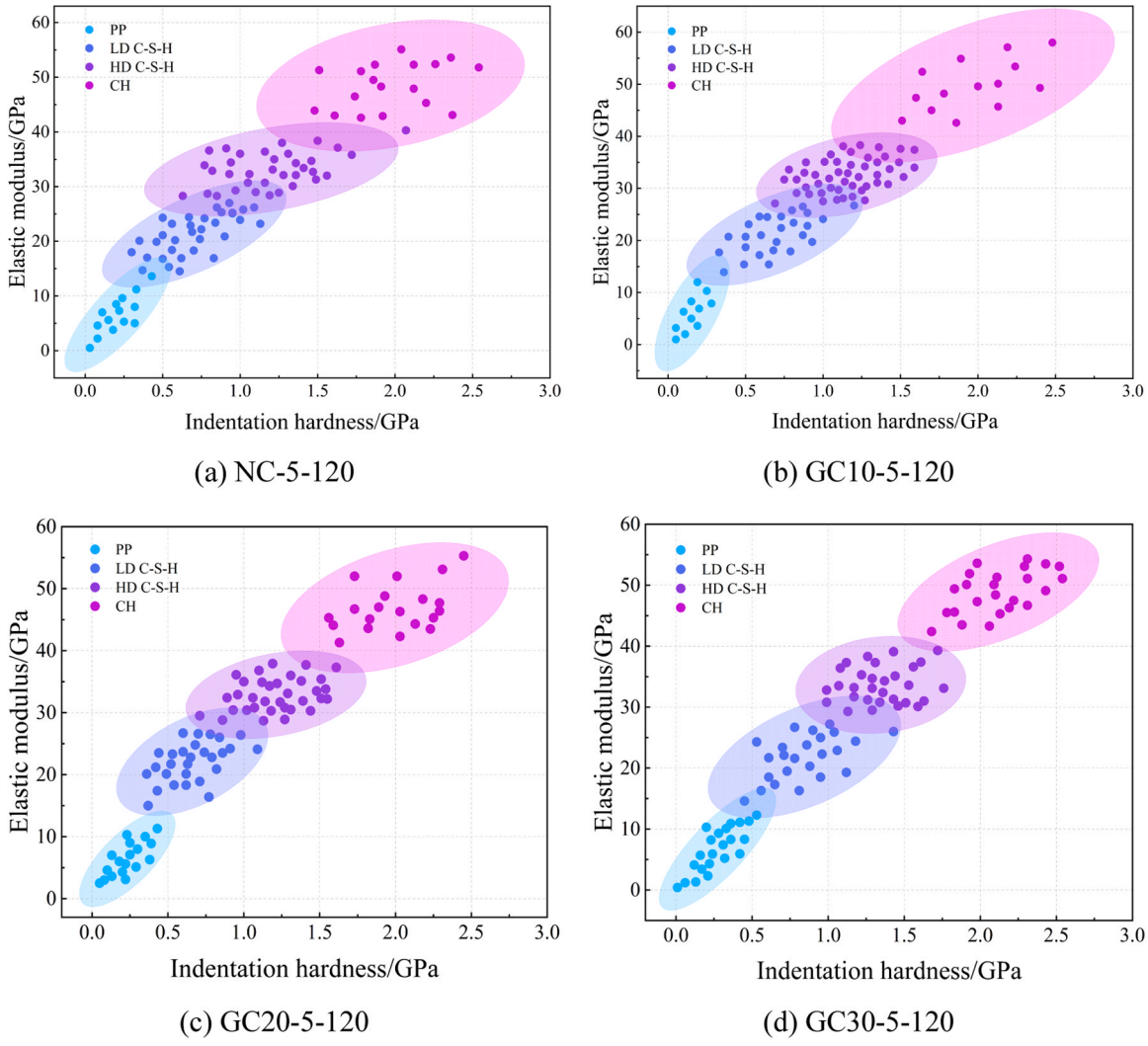

Fig. 17. K-means clustering results for different mortar samples after 120 days of erosion to 5% sodium sulfate solution.

Table 5
Cluster analysis results for the hardness and elastic modulus of different mortar samples.

Sample	Phase	H/GPa	E/GPa	Volume fraction/%
NC	PP	0.21	6.59	14
	LD C-S-H	0.71	21.32	33
	HD C-S-H	1.20	33.16	35
	CH	1.97	48.49	18
GC10	PP	0.16	6.05	11
	LD C-S-H	0.89	23.10	27
	HD C-S-H	1.35	34.55	48
	CH	1.98	49.76	14
GC20	PP	0.23	6.43	18
	LD C-S-H	0.66	22.09	28
	HD C-S-H	1.21	32.90	34
	CH	2.00	46.92	20
GC30	PP	0.27	6.70	22
	LD C-S-H	0.81	21.84	24
	HD C-S-H	1.25	33.65	30
	CH	2.12	48.90	24

those of the GC10 group. When the UGP content increased to 20% and 30%, the micromechanical properties decreased systematically. The volume fractions of the PP phase in the GC20 and GC30 groups increased to 18% and 22%, respectively, while the proportions of the HD C–S–H phase decreased to 34% and 30%, respectively. These findings indicate that for the samples with UGP contents of 20% and 30%, the amount of C−S−H gel produced by the cement hydration reaction was reduced, and a large number of pores were generated inside the samples, which allowed the easy erosion of the sodium sulfate solution and expose the interior of the samples and ultimately led to a decrease in the micromechanical properties.

The results of the nanoindentation test reveal that the addition of an appropriate amount of UGP significantly improved the micromechanical properties of the mortar, whereas an excessively high UGP content deteriorated the internal structure of the sample. By optimizing the type and distribution of the hydration products, the density and micromechanical properties of the samples significantly improved when 10% UGP was added. However, when the UGP content was 20% or 30%, the proportion of the HD C−S−H phase continued to decrease, and the proportion of the PP phase continued to increase, resulting in the degradation of the structural properties of the material at the nanoscale. This is consistent with the macroscopic mechanical properties and SEM and XRD analysis results, which together clarify the mechanism by which the UGP content influences sulfate resistance.

The elastic modulus and hardness phase distribution of each group of samples are shown in Fig. 18 and Fig. 19, respectively. In the figure, the blue area represents the pores inside the sample, the green area represents C−S−H gel, and the yellow and red areas represent calcium hydroxide. As shown in Figs. 18 and 19, the C−S−H gel in the GC10 group had the most uniform distribution and accounted for a significant proportion, indicating that the microstructure of GC10 was dense and that its mechanical properties were stable. In the NC group, the distribution of the C−S−H gel was relatively narrow, and the pore and calcium hydroxide areas increased in size, reflecting the poor structural uniformity of NC. In the GC20 and GC30 groups, many pores and large amounts of calcium hydroxide existed, and a continuous network was formed, which indicates that the micromechanical properties of the samples were severely uneven at high contents and that cracking and expansion easily occurred under stress.

Comprehensive analysis shows that the improvement of sulfate resistance of cement mortar with 10% UGP content is the result of the synergistic effect of volcanic ash chemical reaction and matrix microstructure evolution. The active SiO_2 in UGP reacts with the Ca$(OH)_2$ generated by hydration of cement to produce pozzolanic reaction, which preferentially consumes the core reactant Ca$(OH)_2$ to generate gypsum and ettringite from the chemical reaction level, reduces the formation of expansive erosion products from the source, and promotes the secondary formation of C-S-H gel. SEM microscopic characterization showed that the compactness of the mortar matrix was significantly improved under 10% UGP content, the flake Ca$(OH)_2$ crystals were greatly reduced, the C-S-H gel was uniformly distributed in a continuous network, the number and size of microcracks and pores were significantly reduced, and there was no obvious AFt needle crystal agglomeration. The nanoindentation quantitative test further quantified the optimization effect. The volume fraction of high-density C-S-H phase in GC10 group reached 48%, which was 13% higher than that in NC group, the volume fraction of porous composite phase decreased to 11%, and the Ca$(OH)_2$ phase decreased to 14%. The elastic modulus and hardness of HD C-S-H phase reached 34.55 GPa and 1.35 GPa, respectively, which were 4.2% and 12.5% higher than those of the blank group. The micro-mechanical properties and pore structure refinement effect were significant.

4. Reliability life prediction of cement mortar based on Weibull distribution

4.1. Weibull distribution theory

Due to the heterogeneity of cement-based materials and the complexity as well as variability of the actual service environment, a considerable amount of random and incomplete information is often encountered in predicting the service life of such materials. Therefore, it is necessary to employ probabilistic distribution methods to mitigate the randomness in evaluation parameters and the incompleteness of information, thereby reducing the inaccuracy of prediction results and making the life prediction more realistic and

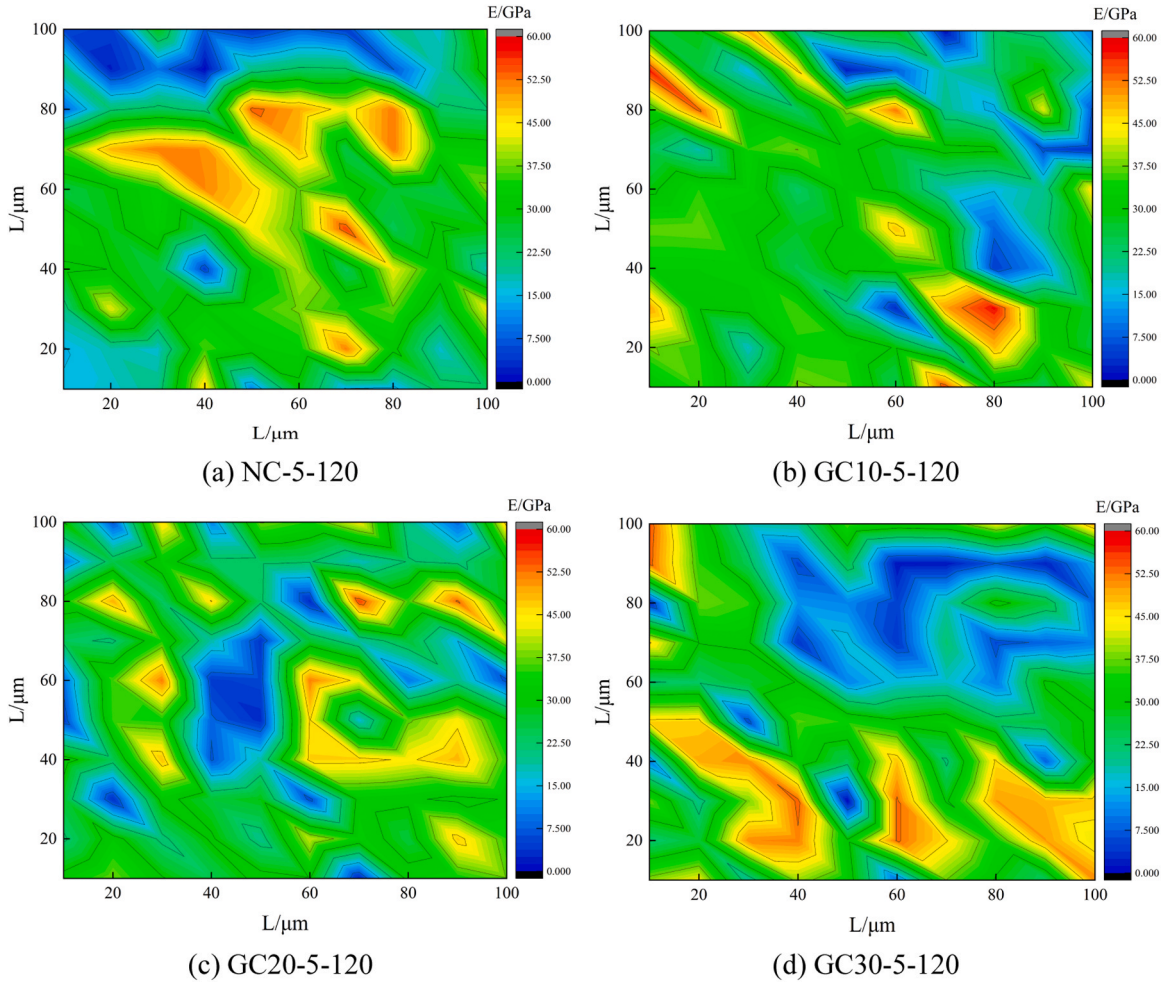

Fig. 18. Phase distribution of elastic modulus of different mortar specimens after immersion in 5% sodium sulfate solution for 120 days.

reliable [48–50]. The reliability modeling approach based on performance degradation data serves as an effective supplement to traditional life prediction methods and provides an important means for addressing life prediction problems in products characterized by small sample sizes, high reliability, and long service life. Among these methods, the Weibull distribution model is relatively straightforward in terms of mathematical processing. Compared with normal and lognormal distribution models, the Weibull distribution model offers a broader scope of application, greater flexibility, and can deliver more accurate life predictions even with a smaller number of samples [51–54]. The two-parameter Weibull distribution function, in particular, demonstrates high accuracy when applied to small sample data. Therefore, this paper adopts a two-parameter Weibull distribution model to predict the durability life of cement mortar samples [55]. It is assumed that the durability life T of cement mortar follows the Weibull distribution, and by estimating the shape and scale parameters, the reliability function of the cement mortar samples can be established.

The two-parameter Weibull distribution function is

$$F(t) = 1 - e^{\left(-\frac{t}{u}\right)^{v}} \tag{12}$$

The reliability function is

$$f(t) = 1 - F(t), 0 < f(t) < 1 \tag{13}$$

where u denotes the scale parameter ($u > 0$), v represents the shape parameter (v > 0), and t indicates the duration of sulfate erosion in days ($t \geq 0$), the reliability of the cement mortar sample exhibits an inverse relationship with its service life. As the sulfate erosion time increases, the reliability of the sample progressively declines. Failure is defined when the reliability drops to zero, and the cumulative number of erosion days at this point corresponds to the service life predicted in this study.

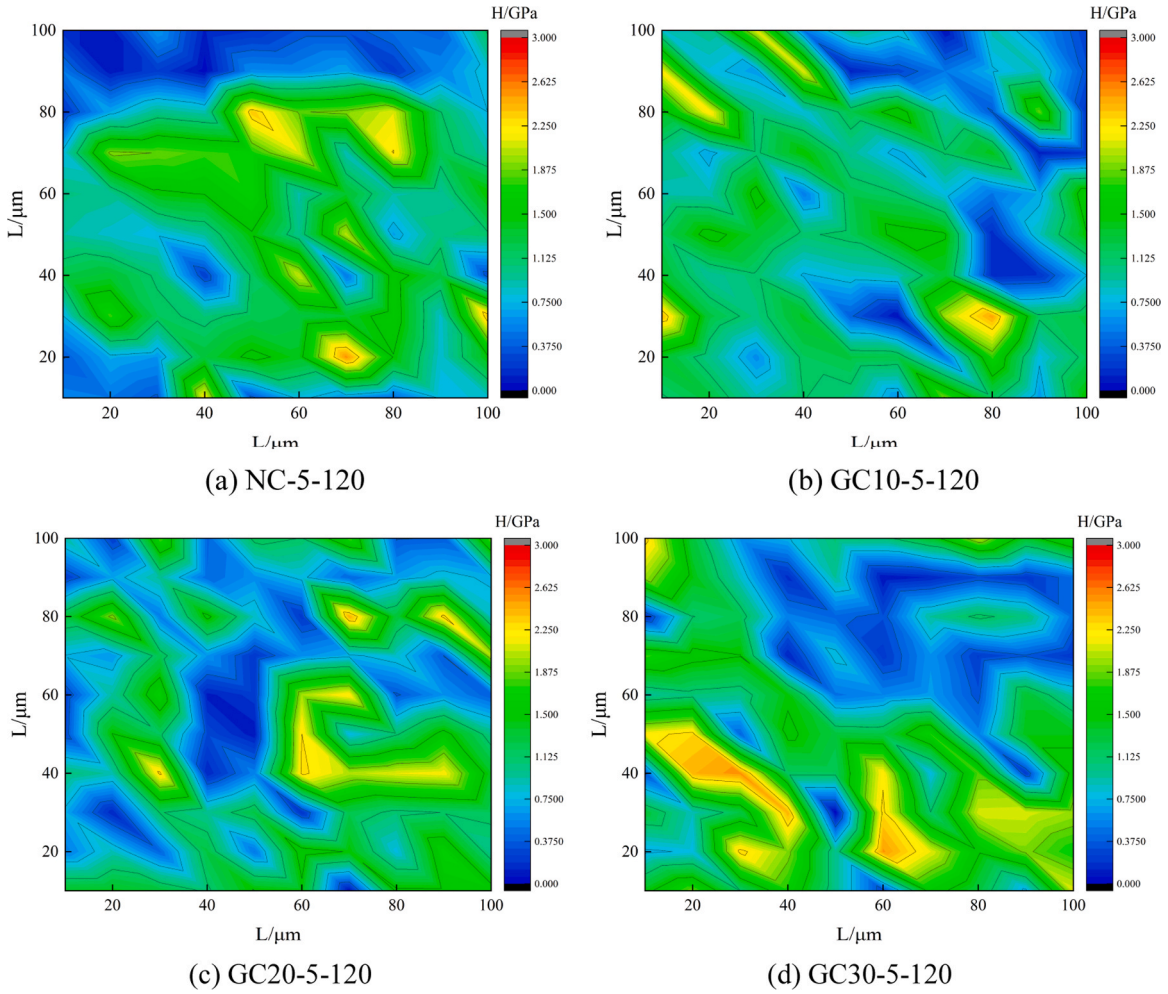

Fig. 19. Phase distribution of hardness of different mortar specimens after immersion in 5% sodium sulfate solution for 120 days.

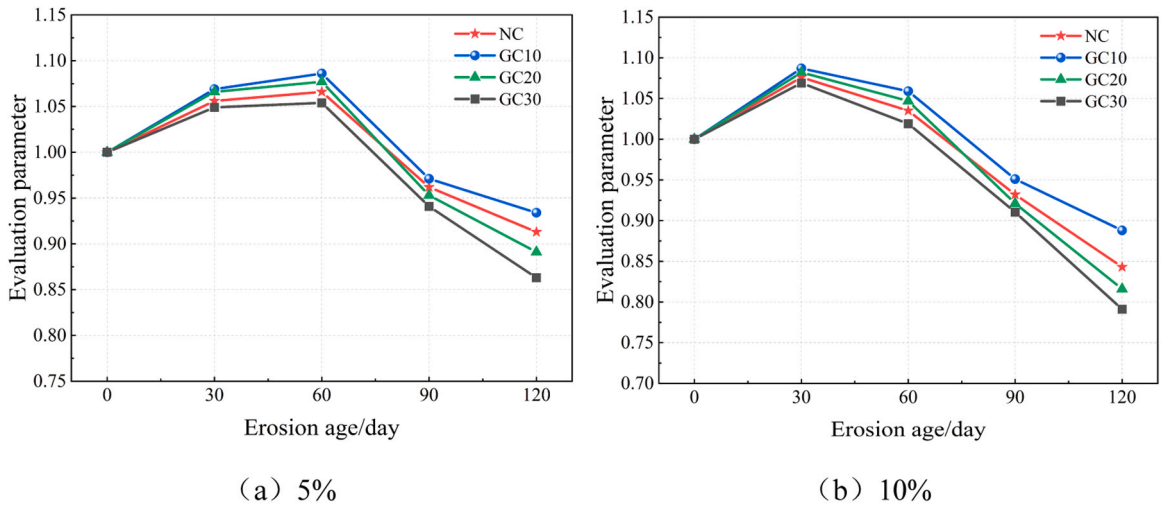

Fig. 20. Variation of the evaluation parameter for relative dynamic elastic modulus of samples with erosion time under erosion in sodium sulfate solutions of different concentrations.

4.2. Parameter estimation of Weibull distribution based on relative dynamic elastic modulus

The evaluation parameter P for the relative dynamic elastic modulus can be calculated using Eq. (14), based on the measured relative dynamic elastic modulus of the sample at various sulfate erosion durations.

$$P = \frac{\frac{E_t}{E_0} - 0.95}{0.05} \tag{14}$$

Where E_t denotes the dynamic elastic modulus measured after t days of sulfate erosion, and E_0 represents the corresponding modulus before the erosion test begins.

Fig. 20 shows the changes in the relative dynamic elastic modulus evaluation parameters of the samples under sulfate attack at different concentrations. With increasing sulfate erosion duration, these parameters initially increase and subsequently decrease. Under 10% concentration sulfate erosion, the peak value of the parameters appears earlier, which is consistent with the variation patterns of flexural strength, compressive strength, and the corrosion resistance coefficient described in Section 3.1. This suggests that during the early stage of sulfate erosion, the erosion products generated within the mortar sample fill the pores, resulting in a denser internal pore structure and thereby improving the relative dynamic elastic modulus. In the later stage of erosion, due to the continuous generation of erosion products, the internal pore pressure of the sample increases and micro-cracks develop. As sulfate erosion continues, these micro-cracks propagate, and the progressive leaching of cementitious materials leads to a reduction in the relative dynamic elastic modulus. For samples eroded by 5% sodium sulfate solution, the relative dynamic elastic modulus parameters reached their peak at 60 days. With further sulfate erosion, these samples began to sustain damage, whereas for samples subjected to 10% sodium sulfate erosion, damage onset occurred at 30 days.

Due to its simplicity and practicality, the least squares method facilitates the calculation of parameters related to linear functions. Therefore, the least squares method is employed to take the logarithm of the reliability function, as shown in Eq. (15).

$$\ln[-\ln f(t)] = v \ln t - v \ln u \tag{15}$$

Let $y = \ln[-\ln f(t)]$ and $x = \ln t$. Then Eq. (14) can be simplified to

$$y = ax + b \tag{16}$$

Where $v = a$, and $u = e^{-\frac{b}{v}}$.

The calculation results of the parameters of the sample are shown in Table 6.

4.3. Reliability analysis and life prediction based on two-parameter Weibull distribution

By substituting the parameters obtained in Table 6 into the reliability function (13), the reliability life prediction curve of cement mortar sample can be obtained, as shown in Fig. 21. Among them, the reliability of NC-5 is basically 0 at 478 days of sulfate attack, and the sample fails, that is, the life of NC-5 is 478 days. The reliability of GC10–5, GC20–5 and GC30–5 is 0 at 515 days, 412 days and 375 days of sulfate attack, respectively, that is, the corresponding life is 515 days, 412 days and 375 days, respectively. It can be seen that when the UGP content is 10%, the life of the cement mortar sample is prolonged, and when the UGP content is 20% and 30%, the life of the cement mortar sample is shortened.

Under the erosion of 10% concentration of sodium sulfate, the reliability of NC-10 is basically 0 at 363 days of erosion, that is, the corresponding life is 363 days; the reliability of GC10–10, GC20–10 and GC30–10 is 0 at 423 days, 338 days and 317 days, respectively, that is, the corresponding life is 423 days, 338 days and 317 days, respectively. This shows that with the increase of the concentration of sodium sulfate solution, the life of each group of samples has decreased, and for the samples with UGP content of 10%, the predicted life remains the highest. It is shown that when the UGP content is 10%, the internal structure of the cement mortar sample is the most compact, which inhibits the generation and expansion of micro cracks in the sample under sulfate attack.

The reliability life of this paper is only the predicted value, which is different from the actual project, but it provides a new idea and certain reference value for the life prediction of ultrafine glass powder cement mortar in sulfate erosion environment. It should be noted that the predicted service lives presented here are based on accelerated laboratory conditions and are intended for comparative

Table 6
Parameters corresponding to the Weibull distribution.

Sample	Shape parameter	Scale parameter
NC-5	2.969	269.017
GC10–5	2.926	300.368
GC20–5	3.039	244.153
GC30–5	3.076	223.614
NC-10	3.080	212.993
GC10–10	2.991	244.651
GC20–10	3.144	199.143
GC30–10	3.186	189.197

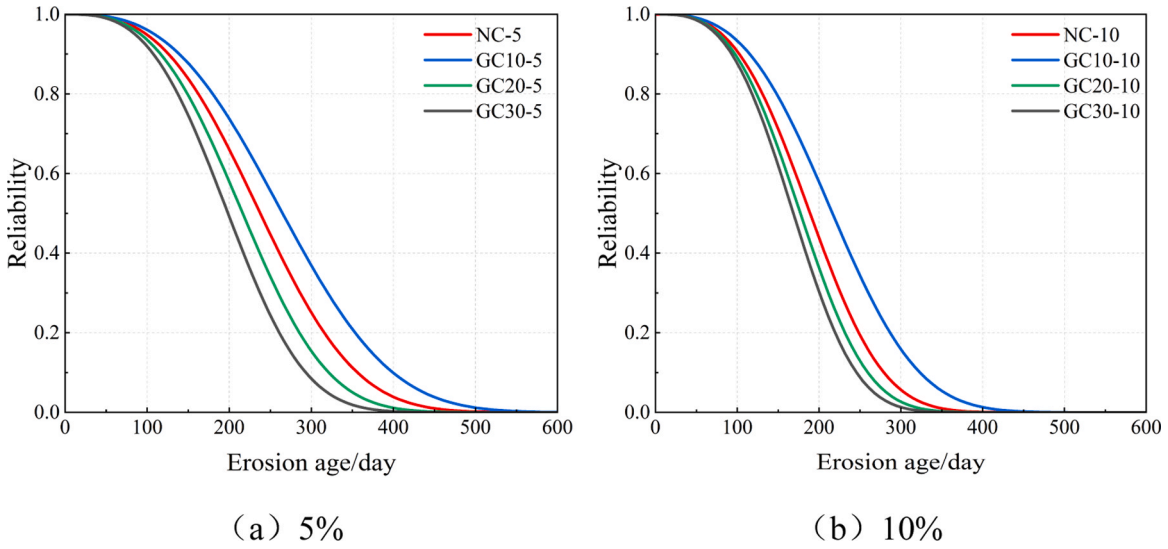

Fig. 21. Reliability life prediction curve of cement mortar samples.

evaluation of material formulations. For real engineering applications, factors such as temperature fluctuations, wet-dry cycles, and loading conditions should be considered to refine the model

5. Conclusion

In this study, the influence of varying content levels of UGP on the sulfate resistance of cement mortar was systematically investigated. Through macroscopic mechanical tests, analysis of mass evolution, SEM, XRD, nanoindentation, and a reliability-based life prediction method grounded in Weibull distribution, the following main conclusions were drawn:

(1) Incorporating an appropriate amount of UGP significantly improves the microstructure and long-term durability of cement mortar. The optimal replacement level was found to be 10%. At this content, UGP effectively refined the pore structure and densified the matrix, as evidenced by a more continuous C–S–H gel distribution and a 48% volume fraction of high-density C–S–H—a marked increase from the control group. This microstructural improvement directly translates to superior macroscopic performance, including reduced mass loss (only 3.2% after 120 days in a 10% sulfate solution) and enhanced resistance to flexural and compressive strength degradation.
(2) The UGP as a by-product with low economic value can be effectively recycled to produce high-performance, durable construction materials. By replacing 10% of the cement with this waste product, the study presents a viable strategy for reducing cement consumption, lowering material costs, and mitigating the environmental impact associated with both cement production and waste landfilling. This approach offers a pathway toward more sustainable and economically efficient concrete production.
(3) A reliability-based life prediction model via Weibull distribution was developed and validated as an effective tool for forecasting material performance. The model's application shows that mortar with 10% UGP has a predicted service life of 515 days and 423 days under 5% and 10% sodium sulfate attack, respectively.

CRediT authorship contribution statement

LI Zhilong: Writing – review & editing, Writing – original draft, Visualization, Data curation. **HOU Dongchang:** Writing – review & editing, Validation, Supervision, Funding acquisition, Conceptualization. **ZHAO Yi:** Supervision, Investigation, Conceptualization. **Yuzhou SUN:** Writing – review & editing, Supervision, Project administration, Funding acquisition, Conceptualization. **WANG Jinyan:** Writing – review & editing, Supervision, Investigation, Funding acquisition, Formal analysis. **ZHOU Xiangming:** Writing – review & editing, Supervision, Investigation, Formal analysis, Conceptualization.

Declaration of Competing Interest

The authors declare that they have no known competing financial interests or personal relationships that could have appeared to influence the work reported in this paper.

Acknowledgements

This work is supported in part by the National Natural Science Foundation of China under Grant No. 12502027, the International Science and Technology Cooperation Project of Henan Province under Grant No. 241111521200. sponsored by the Natural Science Foundation of Henan under Grant No. 252300421796 and Key Research Projects of Higher Education Institutions in Henan Province under Grant No. 25A560002 and the Natural Science Foundation of Zhongyuan University of Technology under Grant No. K2025YB002.

Data availability

Data will be made available on request.

References

[1] J.X. Lu, P. Shen, H. Zheng, B. Zhan, H.A. Ali, P. He, C.S. Poon, Synergetic recycling of waste glass and recycled aggregates in cement mortars: Physical, durability and microstructure performance, Cem. Concr. Compos. 113 (2020) 103632.
[2] A.A. Aliabdo, M. Abd Elmoaty, A.Y. Aboshama, Utilization of waste glass powder in the production of cement and concrete, Constr. Build. Mater. 124 (2016) 866–877.
[3] X. Wang, R. Yu, Z. Shui, Q. Song, Z. Liu, Z. Liu, S. Wu, Optimized treatment of recycled construction and demolition waste in developing sustainable ultra-high performance concrete, J. Clean. Prod. 221 (2019) 805–816.
[4] M.Z. Guo, X. Fei, C. Pei, W. Jin, Environmentally-optimized photocatalytic NOX degradation in cement mortars utilizing recycled red brick and waste glass for sustainable management, J. Environ. Manag. 375 (2025) 124209.
[5] M. Huang, P. Fang, Q. Chen, J. Zhang, J. Duan, Y. Lv, W. Jin, Study on the mechanical properties and damage evolution of basalt fiber shotcrete with alkaline and non-alkaline accelerators under different freeze-thaw media, Constr. Build. Mater. 500 (2025) 144190.
[6] M. Mejdi, W. Wilson, M. Saillio, T. Chaussadent, L. Divet, A. Tagnit-Hamou, Hydration and microstructure of glass powder cement pastes–a multi-technique investigation, Cem. Concr. Res. 151 (2022) 106610.
[7] Q. Pan, L. Peng, Y. Zhao, Mechanisms underlying the long-term reaction in high-volume glass powder cement system, Constr. Build. Mater. 470 (2025) 140627.
[8] T. Wang, R. San Nicolas, A. Kashani, T. Ngo, Sustainable utilisation of low-grade and contaminated waste glass fines as a partial sand replacement in structural concrete, Case Stud. Constr. Mater. 16 (2022) e00794.
[9] D. Paul, K.R. Bindhu, A.M. Matos, J. Delgado, Eco-friendly concrete with waste glass powder: a sustainable and circular solution, Constr. Build. Mater. 355 (2022) 129217.
[10] Y. Zhang, J. Peng, Z. Wang, M. Xi, J. Liu, L. Xu, Machine learning-assisted sustainable mix design of waste glass powder concrete with strength–cost–CO2 emissions trade-offs, Buildings 15 (15) (2025) 2640.
[11] Q. Su, J. Xu, Mechanical properties of rice husk ash and glass powder concrete: experimental and mesoscopic studies, J. Build. Eng. 95 (2024) 110278.
[12] R. Idir, M. Cyr, A. Tagnit-Hamou, Use of fine glass as ASR inhibitor in glass aggregate mortars, Constr. Build. Mater. 24 (7) (2010) 1309–1312.
[13] Q. Li, X. Shi, Y. Hu, C. Kang, X. Zhao, Establishment of hydration kinetics model and micro-mechanism analysis of waste glass powder-cement composite cementitious material under physical activation, J. Build. Eng. (2025) 114306.
[14] Z. Liu, Y. Jiao, Y. Chen, H. Yang, Y. Du, The effect of waste glass powder on the flexural behavior of ultra-high performance concrete: mechanical testing, microscopic observation, and damage evolution, J. Clean. Prod. 532 (2025) 146934.
[15] J. Jin, T. Liu, M. Li, Z. Qin, Y. Chen, Q. Liu, S. Zuo, Influence of biomass fly ash on durability of self-consolidating cement-tailings grout: Resistance to freeze-thaw cycles and sulfate attack, J. Build. Eng. 93 (2024) 109842.
[16] C. Wang, J. Xiao, C. Long, Q. Zhang, J. Shi, Z. Zhang, Influences of the joint action of sulfate erosion and cementitious capillary crystalline waterproofing materials on the hydration products and properties of cement-based materials: a review, J. Build. Eng. 68 (2023) 106061.
[17] Y. Shao, X. Lu, Q. Li, Y. Dong, L. Zhang, C. Jiang, X. Cheng, Study on the preparation and sulfate resistance of Portland cement clinker with the high Fe/Al ratio of ferrite phase, Cem. Concr. Compos. 134 (2022) 104699.
[18] J. Yang, Q. Ding, G. Zhang, D. Hou, M. Zhao, J. Cao, Effect of sulfate attack on the composition and micro-mechanical properties of CASH gel in cement-slag paste: a combined study of nanoindentation and SEM-EDS, Constr. Build. Mater. 345 (2022) 128275.
[19] G. Fu, K. Tang, D. Zheng, B. Zhao, P. Li, G. Yao, X. Li, Effect of cementitious capillary crystalline waterproof material on the resistance of concrete to sulfate erosion, Materials 18 (20) (2025) 4659.
[20] S. Lu, J. Liu, Z. Tian, Y. Lu, G. Liang, L. Zhang, H. Bian, Deterioration mechanisms and strength prediction of hybrid fiber-reinforced concrete under coupled sulfate attack and dry-wet cycles, Constr. Build. Mater. 493 (2025) 143243.
[21] Y. Sun, M. You, X. Yin, D. Hou, J. Li, X. Zhou, Study on the micro-mechanism of corrosion deterioration of concrete under sulfate attack environment, Materials 18 (12) (2025) 2904.
[22] I. Fonseka, D. Mohotti, K. Wijesooriya, C.K. Lee, P. Mendis, Synergistic effects of graphene oxide and fly ash on long-term durability and strength properties of concrete, Constr. Build. Mater. 493 (2025) 143130.
[23] M.S. Pasha, M.F. Aslam, M. Hamza, N.M. Ali, I. Jabbar, S. Ahmed, H.K.J. Abbasi, Sustainable construction: performance analysis of concrete incorporating E-waste plastic aggregates and silica fume, Constr. Build. Mater. 474 (2025) 141103.
[24] J. Li, W. Zha, W. Lv, T. Xu, B. Wang, B. Wang, Mechanical properties and sulfate resistance of basalt fiber-reinforced alkali-activated fly ash-slag-based coal gangue pervious concrete, Case Stud. Constr. Mater. 21 (2024) e03961.
[25] Y. Yao, C. Liu, H. Liu, W. Zhang, T. Hu, Deterioration mechanism understanding of recycled powder concrete under coupled sulfate attack and freeze–thaw cycles, Constr. Build. Mater. 388 (2023) 131718.
[26] M. Kang, Y. Jia, H. Zhang, D. Wang, Effects of fly ash on sulfate resistance of ultra-high performance concrete, Constr. Build. Mater. 501 (2025) 144267.
[27] Z. Ye, X. Qu, J. Li, T. Ye, G. Li, H. Wang, Experimental investigation of the effect of nano silica fume on durability of concrete with close-packing aggregate, Materials 18 (17) (2025) 4061.
[28] A. Deep, P. Sarkar, Durability of copper slag aggregate geopolymer concrete exposed to acid and sulphate attack, Constr. Build. Mater. 493 (2025) 143107.
[29] L. Peng, Y. Zhao, J. Ban, Y. Wang, P. Shen, J.X. Lu, C.S. Poon, Enhancing the corrosion resistance of recycled aggregate concrete by incorporating waste glass powder, Cem. Concr. Compos. 137 (2023) 104909.
[30] A.M. Tahwia, M. Abdellatief, M. Abd Elrahman, Durability and ecological assessment of low-carbon high-strength concrete with short AR-glass fibers: effects of high-volume of solid waste materials, Constr. Build. Mater. 429 (2024) 136422.
[31] Q. Cao, B. Han, L. Chen, Z. Liu, Q. Yuan, K. Zheng, Mitigation effect of glass powder on external sulfate attack and its relation to alkalinity of pore solution, Constr. Build. Mater. 370 (2023) 130669.
[32] GB/T 749-2008, Test method for determining capability of resisting sulfate corrode of cement. General Administration of Quality Supervision, Inspection and Quarantine of the People's Republic of China, National Standardization Administration, Beijing, China, 2008.
[33] GB/T 17671-2021; Test method of cement mortar strength (ISO method). State Administration for Market Regulation, National Standardization Administration: Beijing, China, 2021.

[34] W.C. Oliver, G.M. Pharr, An improved technique for determining hardness and elastic modulus using load and displacement sensing indentation experiments, J. Mater. Res. 7 (6) (1992) 1564–1583.
[35] W.C. Oliver, G.M. Pharr, Measurement of hardness and elastic modulus by instrumented indentation: advances in understanding and refinements to methodology, J. Mater. Res. 19 (1) (2004) 3–20.
[36] H.S. Park, C.H. Jun, A simple and fast algorithm for K-medoids clustering, Expert Syst. Appl. 36 (2) (2009) 3336–3341.
[37] Z. Zhang, J. Qin, Z. Ma, X. Pang, Y. Zhou, Comparison of three different deconvolution methods for analyzing nanoindentation test data of hydrated cement paste, Cem. Concr. Compos. 138 (2023) 104990.
[38] S. Wang, C. Liu, S. Xing, Review on K-means clustering algorithm, J. East China Jiaotong Univ. 39 (05) (2022) 119–126.
[39] Y. Chen, P. Liu, Z. Yu, Study on degradation of macro performances and micro structure of concrete attacked by sulfate under artificial simulated environment, Constr. Build. Mater. 260 (2020) 119951.
[40] G. Deng, Y. He, L. Lu, F. Wang, S. Hu, Pore structure evolution and sulfate attack of high-volume slag blended mortars under standard curing and steam curing, Constr. Build. Mater. 363 (2023) 129878.
[41] R. Wen, S. Sun, R. Zhao, W. Xing, J. Liang, Effects of sulfate attack on phase composition and pore structure of cement-based materials, J. Build. Mater. 28 (10) (2025) 966–973.
[42] Z. Yang, C. Zhou, Mechanical properties and microstructure of ultra-high performance concrete containing glass powder, Bull. Chin. Ceram. Soc. 40 (12) (2021) 3956–3963.
[43] N. Schwarz, H. Cam, N. Neithalath, Influence of a fine glass powder on the durability characteristics of concrete and its comparison to fly ash, Cem. Concr. Compos. 30 (6) (2008) 486–496.
[44] Gołek, New insights into the use of glass cullet in cement composites-Long term examinations, Cem. Concr. Compos. 133 (2022) 104673.
[45] H.A. Elaqra, I.H. Elmasry, A.M. Tabasi, M.D. Alwan, H.N. Shamia, M.I. Elnashar, Effect of water-to-cement ratio and soaking time of waste glass powder on the behaviour of green concrete, Constr. Build. Mater. 299 (2021) 124285.
[46] Z. Chen, Y. Wang, S. Liao, Y. Huang, Grinding kinetics of waste glass powder and its composite effect as pozzolanic admixture in cement concrete, Constr. Build. Mater. 239 (2020) 117876.
[47] S. Yu, S. Wu, Y. Zhao, H. Yang, Experimental study of sulfate erosion resistance of cementitious sand with waste glass powder, Buildings 13 (8) (2023) 2037.
[48] C.J. Jiao, C.G. Lu, X.C. Zhang, X.F. Chen, Reliability life analysis of reinforced concrete structures (RCS) in salt corrosion environments: an application of the three-parameter weibull distribution model, Case Stud. Constr. Mater. (2025) e05543.
[49] D. Zhou, D. Chen, F. Yang, J. Mei, Y. Yao, Y. Deng, Freeze–thaw damage analysis and life prediction of modified pervious concrete based on Weibull distribution, Case Stud. Constr. Mater. 20 (2024) e03305.
[50] J. Wang, F. Han, Q. Liu, Research on freeze-thaw damage and life prediction model of polyethylene fiber-reinforced cementitious composites based on reliability analysis, Case Stud. Constr. Mater. 20 (2024) e03049.
[51] Y. Yao, C. Liu, H. Liu, W. Zhang, T. Hu, Deterioration mechanism understanding of recycled powder concrete under coupled sulfate attack and freeze–thaw cycles, Constr. Build. Mater. 388 (2023) 131718.
[52] K. Deng, R. Song, B. Lou, D. Uhm, D. Arola, Improving the strength and reliability of mortar composites with zeolite substitution, Case Stud. Constr. Mater. 21 (2024) e04037.
[53] Y. Yang, P. Gao, B. Zhan, Q. Yu, J. Wang, Y. Zhang, Influence of limestone powder particle size on the sulfate resistance of cement-based materials under the coupling effect of time-varying temperature and sulfate attack, J. Build. Eng. 98 (2024) 111271.
[54] Y. Jiang, H. Liu, H. Liu, J. Che, W. Yang, Experimental study on the uniaxial compressive mechanical properties of desert sand concrete after sulfate freeze-thawing, Mater. Rep. 39 (07) (2025) 119–129.
[55] C. Lu, Z. Wei, H. Qiao, G. Qiao, Y. Fu, Durability life prediction of reinforced concrete in corrosive environment based on weibull distribution, J. Basic Sci. Eng. 30 (06) (2022) 1534–1544.